Nano Research

ISSN 1998-0124 CN 11-5974/O4
https://doi.org/10.26599/NR.2026.94909224

Research Article

Tuning Mn–O covalency by ion intercalation to boost the oxidase-like activity of birnessite

Yao-Yao Chen[1,2], Bo-Han Yao[1,2], Qi-Lin Zhao[1,2], Li-Min Ma[1,2], Rui Han[1,2], Dong-Ming Xu[1,2], Chun-Xia Ma[1,2], Bing Zhang[1,2], Zhi-Ying Jin[1,2], Dong-Xu Jiao[3], Huan-Huan Xing[4], De-Wen Wang[1](✉), Xiu-Rong Yang[1,2](✉)

[1] State Key Laboratory of Electroanalytical Chemistry, Changchun Institute of Applied Chemistry, Chinese Academy of Sciences, Changchun 130022, China

[2] School of Applied Chemistry and Engineering, University of Science and Technology of China, Hefei 230026, China

[3] College of Chemistry, Chemical Engineering and Resource Utilization, Northeast Forestry University, Harbin 150040, China

[4] School of Materials Science and Engineering, Suzhou University of Science and Technology, Suzhou 215009, China

Nano Res., **Just Accepted Manuscript** • https://doi.org/10.26599/NR.2026.94909224

https://www.sciopen.com/journal/1998-0124 on Sep. 28, 2026

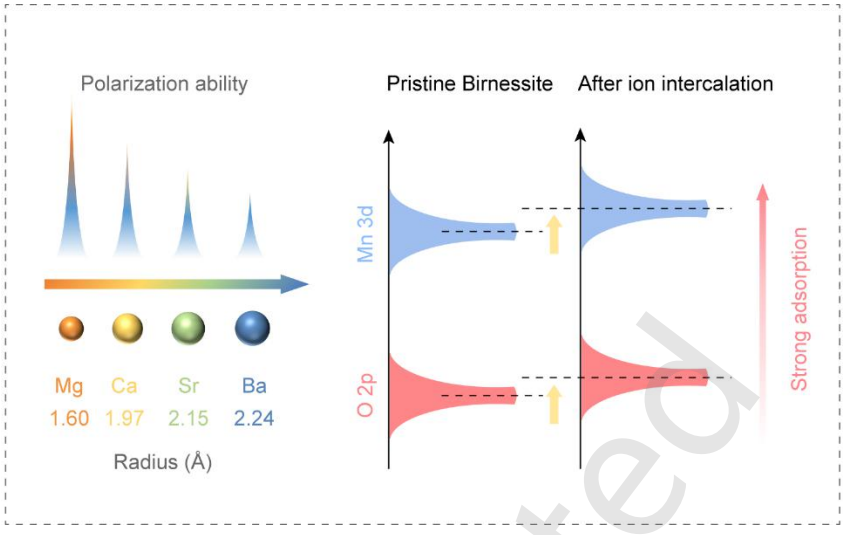
© The Authors(s)

Just Accepted

This is a "Just Accepted" manuscript, which has been examined by the peer-review process and has been accepted for publication. A "Just Accepted" manuscript is published online shortly after its acceptance,which is prior to technical editing and formatting and author proofing. Tsinghua University Press (TUP) provides "Just Accepted" as an optional and free service which allows authors to make their results available to the research community as soon as possible after acceptance. After a manuscript has been technically edited and formatted, and the page proofs have been corrected, it will be removed from the "Just Accepted" web site and published officially with volume and article number (e.g., *Nano Research*, **2025**, *18*, 94906990). Please note that technical editing may introduce minor changes to the manuscript text and/or graphics which may affect the content, and all legal disclaimers that apply to the journal pertain. In no event shall TUP be held responsible for errors or consequences arising from the use of any information contained in these "Just Accepted" manuscripts. To cite this anuscript please use its Digital Object Identifier (DOI®),which is identical for all formats of publication.

Just Accepted

TABLE OF CONTENTS (TOC)



The catalytic performance of metal oxide-based nanozymes remains limited, and the influence of the intrinsic properties of metal–oxygen bonds has yet to be explored. This study demonstrates an ion intercalation strategy that effectively modulates the Mn–O covalency in Birnessite. The upshifted Mn 3*d* and O 2*p* band centers optimize substrate adsorption and electron transfer processes, resulting in superior oxidase-like activity.

Just Accepted

Nano Research

Open Access

Research Article

Tuning Mn–O covalency by ion intercalation to boost the oxidase-like activity of birnessite

Yao-Yao Chen,[1,2] Bo-Han Yao,[1,2] Qi-Lin Zhao,[1,2] Li-Min Ma,[1,2] Rui Han,[1,2] Dong-Ming Xu,[1,2] Chun-Xia Ma,[1,2] Bing Zhang,[1,2] Zhi-Ying Jin,[1,2] Dong-Xu Jiao,[3] Huan-Huan Xing,[4] De-Wen Wang,✉[,1] and Xiu-Rong Yang✉[,1,2]

[1] *State Key Laboratory of Electroanalytical Chemistry, Changchun Institute of Applied Chemistry, Chinese Academy of Sciences, Changchun 130022, China*
[2] *School of Applied Chemistry and Engineering, University of Science and Technology of China, Hefei 230026, China*
[3] *College of Chemistry, Chemical Engineering and Resource Utilization, Northeast Forestry University, Harbin 150040, China*
[4] *School of Materials Science and Engineering, Suzhou University of Science and Technology, Suzhou 215009, China*

Received: 12 July 2026; **Revised:** 3 September 2026; **Accepted:** 28 September 2026

✉Address correspondence to Xiu-Rong Yang, xryang@ciac.ac.cn; De-Wen Wang, dwwang@ciac.ac.cn

Cite this article: *Nano Research*, 2026, 19, 94909224 https://doi.org/10.26599/NR.2026.94909224

ABSTRACT: Most previous efforts have concentrated on extrinsic structural modification to elucidate the catalytic behavior of metal oxide nanozymes, while the influence of intrinsic metal–oxygen (M–O) bonding properties remains underexplored. Herein, we report an ion-intercalation strategy to tailor the Mn–O covalency in layered Birnessite. The polarization effect induced by intercalated alkaline-earth ions (Mg^{2+}, Ca^{2+}, Sr^{2+}, Ba^{2+}) strengthens the Mn–O bond. This effect synergistically optimizes the electronic structure of both Mn and O sites, evident from the accumulated electron density and upshifted band centers. This enhancement endows the nanozyme with a superior oxidase-like activity, featuring a higher specific activity, improved substrate affinity, and accelerated reaction kinetics. Mechanistic studies reveal that the strengthened covalency facilitates substrate adsorption, promotes electron transfer and O–O bond dissociation, and lowers the energy barrier for the rate-determining step. Leveraging this performance, a colorimetric sensor array was constructed for the precise identification of five antioxidants (TA, AA, EGC, GA, CYS). This work elucidates the pivotal role of metal–oxygen covalency in catalysis and establishes a novel paradigm for the electronic-structure engineering of high-performance nanozymes.

KEYWORDS: interlayer engineering, ion intercalation, covalency regulation, oxidase (OXD)-like activity, colorimetric sensor array

1 Introduction

Nanozymes are class of nanomaterial-based artificial enzymes, with catalytic activities and kinetics comparable to those of natural enzymes [1-4]. Since the initial discovery of the intrinsic enzyme-mimicking property of Fe_3O_4 nanoparticles by Yan et al. in 2007, metal oxide-based nanozymes have emerged as promising substitutes for natural enzymes owing to their excellent electronic properties, remarkable stability under harsh conditions, and tunable physicochemical characteristics [5-6]. However, their further development remains constrained by generally low intrinsic activities and an insufficient understanding of catalytic mechanisms [7]. Consequently, numerous strategies including morphology/size control, surface modification and defect/coordination engineering have been pursued to enhance their catalytic performance [8-13]. Yet, these conventional approaches mainly focus on extrinsic structural modifications, often neglecting the critical influence of intrinsic metal–oxygen (M–O) bonding properties on catalytic behavior.

The catalytic activity and reaction pathways of enzyme mimics are fundamentally governed by the electronic structure at the catalyst surface [14-15]. For metal oxide-based nanozymes, M–O covalency serves as a key descriptor, as it directly modulates charge distribution between metal and oxygen atoms and thereby tailors the electronic and band structure [16]. A well-optimized electronic environment promotes sufficient substrate adsorption and efficient electron transfer, which are both essential for activating substrates in enzyme-like catalysis [17]. The strategic tuning of M–O covalency has already proven effective in other metal-oxide systems, such as perovskite and spinel oxides [18-20]. For example, introducing N and F into Co_3O_4 enhances the hybridization between Co 3*d* and O 2*p* orbitals, strengthening Co–O covalency, activating lattice oxygen, and reducing the energy barrier for intermediate adsorption [21]. Elucidating the regulatory mechanism of M–O covalency and establishing its structure–activity relationship with the electronic structure of active centers, adsorption/desorption behavior of reaction intermediates, and interfacial electron transfer efficiency is the key to overcoming the inherent limitations of metal oxide-based nanozymes.

Birnessite is a naturally occurring layered manganese oxide, featuring a two-dimensional structure held together by strong in-plane Mn–O covalent bonds and weak interlayer van der Waals interactions [22]. Within each layer, edge-sharing [MnO_6] octahedra form negatively charged sheets, while the van der Waals gaps between adjacent layers allow the insertion of foreign ions or molecules [23]. The intercalation process can

Just Accepted

typically be accomplished via ion exchange at room temperature without disrupting the host structure, offering a mild yet effective route to precisely tune the structure and electronic properties of the [MnO_6] frameworks [24]. Given the structural analogy between the [MnO_6] octahedra in Birnessite and the metal sites in spinel oxides, Mn–O covalency is expected to play a key role in governing its catalytic activity [20]. Considering the structural features and the methodological advantages, intercalation represents a rational strategy to modulate Mn–O bonding. Notably, alkaline-earth metal ions (Mg^{2+}, Ca^{2+}, Sr^{2+}, Ba^{2+}) exhibit systematically varying ionic potentials, which produce periodic polarization effects, making them ideal intercalants for tailoring Mn–O covalency in Birnessite [25].

In this work, we develop an ion intercalation strategy to investigate how Mn–O covalency governs OXD-like activity of Birnessite and clarify its mechanistic origin. By inserting alkaline earth metal ions (Mg^{2+}, Ca^{2+}, Sr^{2+}, Ba^{2+}) with periodic polarization capabilities into the interlayer spaces of Birnessite, we successfully constructed Mn–O bonds with tunable strength. The theoretical and experimental analyses confirm that the covalency of Mn–O bonds are enhanced by the polarization effects of the intercalated ions. This strengthening synergistically optimizes the electronic and band structures: electron density accumulates around Mn and O atoms, accompanied by an upward shift in the Mn 3*d* and O 2*p* band centers. Density functional theory (DFT) calculations further reveal that this covalency regulation promotes substrate adsorption (TMB and O_2), facilitates electron transfer from Mn to O_2, accelerates O–O bond dissociation, and reduces the energy barrier for H_2O desorption. Compared with pristine Birnessite, Mg-intercalated Birnessite (MgBir) exhibits an increased specific activity, improved substrate affinity, and accelerated reaction kinetics, underscoring the crucial role of covalency tuning. Leveraging this enhanced OXD-like performance, we developed a colorimetric sensor array for discriminating five antioxidants (tannic acid (TA), L-ascorbic acid (AA), (-)-Epigallocatechin (EGC), gallic acid (GA) and L-Cysteine (CYS)). Our findings establish a new paradigm for understanding how intrinsic M–O bonding characteristics govern catalytic behavior, paving the way for the rational design of high-performance metal-based nanozymes.

2 Results and discussion

2.1 Theoretical investigations

The Group 2 alkaline earth metal ions (Mg^{2+}, Ca^{2+}, Sr^{2+}, Ba^{2+}) exhibit progressively larger ionic radii across successive periods. Under a constant charge state, their polarization ability, quantified by the ionic potential

$$\Phi = (Z - \sigma)/r \quad (1)$$

(where Z is the charge number, σ is the screening constant, and r is the ionic radius), is inversely proportional to ionic radius [25]. As a result, the polarization effect on intralayer Mn–O bonds decreases in the order: $Mg^{2+} > Ca^{2+} > Sr^{2+} > Ba^{2+}$, governing the trend in covalency regulation. A series of DFT calculations were conducted to theoretically reveal the evolution of Mn–O covalency induced by ion intercalation. In contrast to pristine Birnessite, the ion-intercalated derivatives are labeled as MgBir, CaBir, SrBir, and BaBir, respectively. The computed bond lengths decrease sequentially from Birnessite (1.918 Å) to BaBir (1.892 Å), SrBir (1.891 Å), CaBir (1.886 Å), and MgBir (1.869 Å) (Figure 1a). Concurrently, Bader charges increase along the same series. This simultaneous bond contraction and charge accumulation indicate strengthened orbital interactions and elevated Mn–O covalency [26]. The crystal orbital Hamilton population (COHP) integrals up to the Fermi level quantify the Mn–O bond strength, where a larger magnitude of −COHP values signifying more pronounced covalency (Figure 1b). Specifically, the integrated −COHP values at the Fermi level (E_f) increase in magnitude from −0.62 for Birnessite to −0.66 (BaBir), −0.70 (SrBir), −0.73 (CaBir), and −0.78 (MgBir). These results confirm that the introduction of interlayer ions positively regulates Mn–O bond strength, consistent with the bond length and Bader charge analyses [21, 27]. Moreover, the reinforced Mn–O covalency disrupts local charge balance, promoting the formation of charge-compensating oxygen vacancies [16]. The calculated oxygen vacancy formation energies (Figure 1c) decrease from Birnessite (3.74 eV) to MgBir (3.43 eV). This result confirms that stronger Mn–O bonding thermodynamically favors spontaneous oxygen vacancy formation, providing ancillary support for the enhanced covalency induced by ion intercalation.

To elucidate the influence of intercalation on the electronic band structure, we analyzed the projected density of states (PDOS) of the Mn 3*d* and O 2*p* orbitals. After ion intercalation, the increased overlap between the Mn 3*d* band and the O 2*p* band points to a strengthened Mn−O orbital hybridization (Figure S1). PDOS analysis reveals high electron occupancy near the Fermi level and notable upward shifts of the O 2*p* and Mn 3*d* band centers in comparison to the pristine Birnessite (Figure 1d and 1e) [21, 28]. The closer proximity of both the *d*-band and *p*-band centers to the Fermi level (Figure 1f) facilitates the electron transfer during catalysis [14]. Moreover, with the upward shift of the *d*-band and *p*-band, more antibonding states migrate above the Fermi level, reducing the electron filling and thereby enhancing the bonding interaction with adsorbed substrate [29]. Collectively, theoretical calculations confirm that intercalating alkaline-earth metal ions successfully strengthens the Mn–O bond and optimizes the electronic band structure of both Mn 3*d* and O 2*p* orbitals, thereby regulating the catalytic properties of Birnessite.

Just Accepted

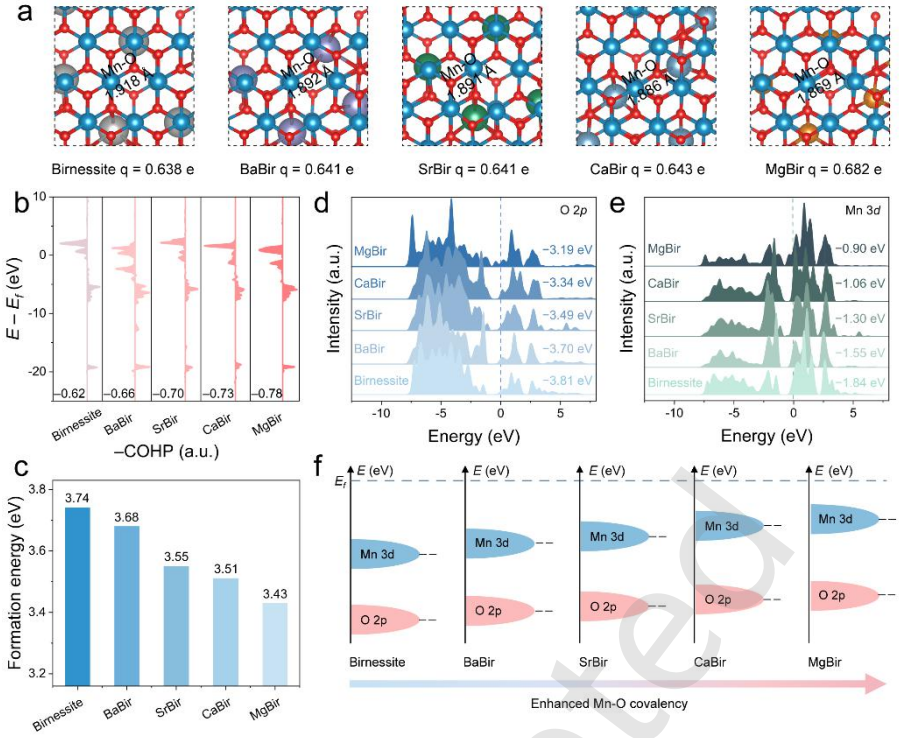


Figure 1. Proposed covalency regulation strategy achieved by ions intercalation. The calculated (a) Bond lengths and Bader charges, (b) Crystal orbital Hamilton population (–COHP), (c) Oxygen vacancy formation energies, (d) PDOS of Mn 3*d* orbit, and (e) PDOS of O 2*p* orbit for Birnessite, BaBir, SrBir, CaBir, and MgBir, respectively. (f) Schematic representation of the Mn 3*d* and O 2*p* band centers obtained by theoretical calculations, E_f represents the Fermi leve

2.2 Catalysts synthesis and structural characterizations

To validate the theoretical predictions, pristine Birnessite was synthesized via a one-step hydrothermal method [30]. Subsequent ion exchange in MCl_2 solutions (M = Mg, Ca, Sr, Ba) introduced alkaline-earth metal ions into the interlayer spaces, yielding the corresponding derivatives. The morphology and microstructure were characterized by scanning and transmission electron microscopy (SEM/TEM). The pristine Birnessite exhibited a three-dimensional flower-like architecture composed of two-dimensional nanosheets (Figure 2a), with an average diameter of 617.54 ± 0.54 nm (Figure S2) [22]. This flower-like morphology was well preserved after ion intercalation (Figure 2b-e). High-resolution TEM (HR-TEM) of pristine Birnessite revealed distinct lattice fringes of 2.27 Å, corresponding to the (100) plane (Figure S3a). In contrast, the ion-intercalated samples showed blurred fringes (Figure S3b-e), indicating intercalant-induced lattice distortion, which theoretical calculations attribute to the generation of oxygen vacancies [14]. Energy-dispersive X-ray (EDX) mapping confirmed the homogeneous distribution of Mg, Ca, Sr, and Ba in their respective samples, and inductively coupled plasma optical emission spectrometry (ICP-OES) provided quantitative incorporation ratios (Table S1).

X-ray diffraction (XRD) confirmed the crystal structure of the samples. The pattern of pristine Birnessite matched the standard for hexagonal Birnessite (PDF#13-0105), with characteristic peaks at 12.2°, 24.7°, 36.8°, and 66.1° indexed to the (001), (002), (100), and (110) planes, respectively (Figure 2f) [23]. The d-value ratio of (100) to (110) planes was approximately 1.73, confirming hexagonal symmetry [31-32]. All ion-intercalated samples retained this structure without impurity phases, as evidenced by consistent peak positions. The interlayer spacing of the (001) plane varied by ≤0.03 Å compared to the pristine sample, indicating structural stability. Fourier-transform infrared (FT-IR) spectroscopy further confirmed the structure, showing Mn–O vibration peaks at 506 and 436 cm^{-1} (Figure S4) [33].

Dynamic light scattering (DLS) measured strongly negative zeta potentials of approximately −25 mV for all samples (Figure 2g), a result of the negatively charged [MnO_6] layers that confer excellent colloidal stability [22]. Brunauer-Emmett-Teller (BET) analysis revealed Type I N_2 adsorption-desorption isotherms, characteristic of non-porous solids (Figure S5). The specific surface area and pore diameter of pristine Birnessite were 137.7 $m^2\ g^{-1}$ and 3.82 nm, respectively. After ion exchange, the surface areas of MgBir, CaBir, SrBir, and BaBir decreased slightly to 103.3, 108.6, 103.9, and 116.9 $m^2\ g^{-1}$, respectively, suggesting mild nanoparticle aggregation [33]. Based on the aforementioned structural characterization, a lattice model with edge-sharing [MnO_6] octahedra, layered two-dimensional structure and ions (Mg^{2+}, Ca^{2+}, Sr^{2+}, Ba^{2+}) intercalation was proposed to graphically represent the crystal structure (Figure 2h). Collectively, these results confirm the successful synthesis of Birnessite and its ion-intercalated derivatives with well-defined structural properties.

Just Accepted

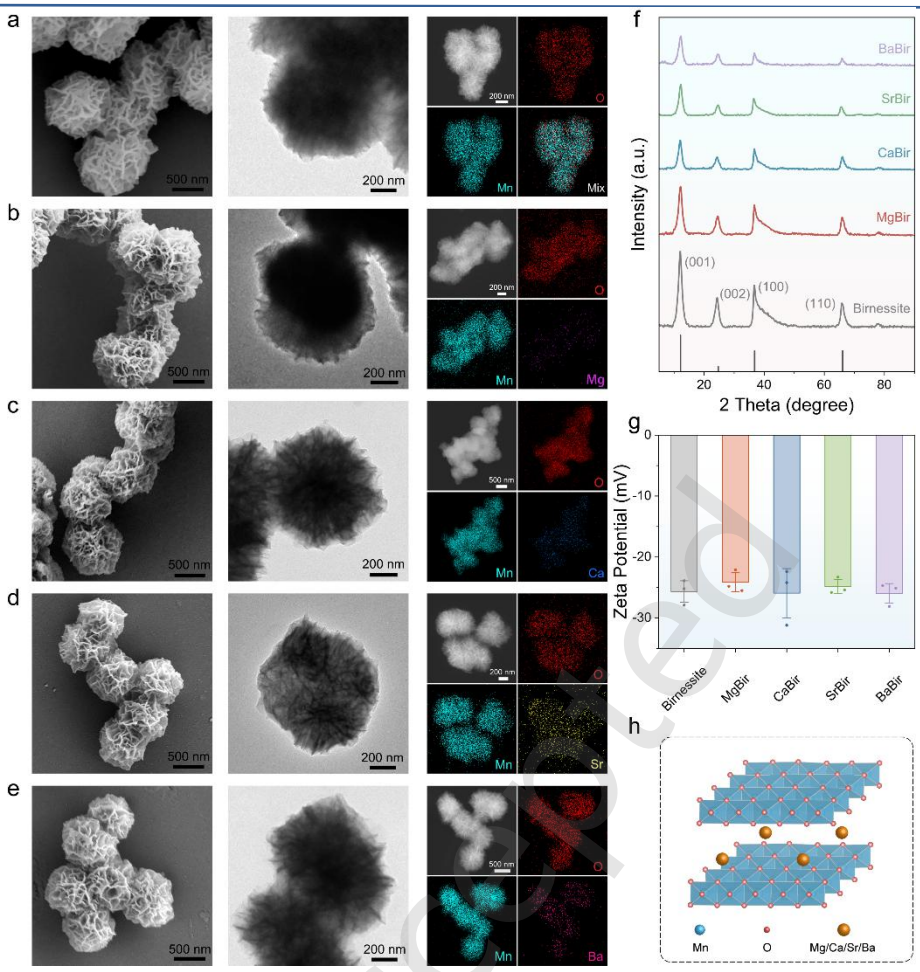


Figure 2. Morphological and structural characterizations. SEM, TEM and EDX elemental mapping images of (a) Birnessite, (b) MgBir, (c) CaBir, (d) SrBir, and (e) BaBir. (f) The XRD patterns. (g) Zeta potential values. (h) Schematic diagram of the crystal structure.

2.3 Electronic structure and coordination environment analysis

X-ray photoelectron spectroscopy (XPS) was employed to probe the surface composition and chemical states of the catalysts. The wide-scan spectra (Figure S6 and Figure S7) confirmed the presence of O and Mn, while high-resolution scans of Mg 1*s*, Ca 2$p_{3/2}$, Sr 3$d_{5/2}$ and Ba 3$d_{5/2}$ revealed distinct signals at binding energies of 1303.1 eV, 346.9 eV, 133.4 eV, and 779.8 eV, respectively [25]. These signals, attributable to the corresponding alkaline-earth metals, provide direct evidence for the successful intercalation of these ions, corroborating the EDS findings. As shown in Figure 3a, the high-resolution O 1*s* spectra were deconvoluted into three components using a mixed Gaussian-Lorentzian function, corresponding to lattice oxygen (O_I, ~530.2 eV), oxygen vacancies (O_{II}, ~531.8 eV), and adsorbed water species (O_{III}, ~533.3 eV) [14, 19]. A notable negative shift of 0.35 eV in the O_I peak position (from 530.33 eV in Birnessite to 529.98 eV in MgBir) indicates enhanced electron density around oxygen atoms, consistent with the strengthened Mn–O covalency induced by intercalation [21]. Concurrently, the concentration of O_{II} (Figure 3b) increased from 9.50% in Birnessite to 17.02% in MgBir. Further validation is provided by the electron paramagnetic resonance (EPR) signals at g = 2.002 (Figure 3c), which serves as a fingerprint of oxygen vacancy [34-35]. This result aligns with DFT predictions, wherein intensified Mn–O covalency disrupts local charge balance, promoting the formation of charge-compensating oxygen vacancies. In the Mn 2*p* XPS spectra (Figure 3d), the peaks at approximately 642 eV (Mn 2$p_{3/2}$) and 654 eV (Mn 2$p_{1/2}$) collectively exhibited a negative binding energy shift from Birnessite to MgBir. Detailed fitting of the Mn 2$p_{3/2}$ spectra (Figure S8) quantified the relative amounts of Mn^{3+} and Mn^{4+} species [33, 36]. The results demonstrate that as the polarizing power of the intercalated ions increases, the Mn^{3+} content rises while the Mn^{4+} content declines [21]. Consequently, the average Mn oxidation state decreased from 3.75 in Birnessite to 3.57 in MgBir (Figure 3e). This reduction confirms that Mn atoms attain a more electron-rich environment upon the strengthening of the Mn–O bond, completing the picture of intercalation-modulated electronic restructuring.

X-ray absorption spectroscopy (XAS) was conducted to further elucidate the coordination environment and electronic structure of the catalysts. The Mn *K*-edge X-ray absorption near edge structure (XANES) spectra (Figure 3f) of all samples show a characteristic double-hump pre-edge feature at ~6542 and 6544 eV, arising from quadrupole-allowed 1*s* to 3*d* transitions [37]. The resolved doublet reflects octahedral crystal field splitting (between e_g and t_{2g} orbitals), confirming the octahedral coordination in [MnO_6]. The white-line peaks near 6562 eV correspond to the dipole-allowed 1*s* to 4*p* transition and is sensitive to the Mn oxidation state, with its intensity decreasing [38]. Such intensity evolution indicates a progressive reduction in the average Mn oxidation state from Birnessite to MgBir, which aligns with the valence trend derived from XPS analysis. The results collectively confirm that the increasing polarization

Under Accepted

ability of the intercalated ions effectively remodels the electronic state of Mn. The local structure was further probed by analyzing the Mn *K*-edge extended X-ray absorption fine structure (EXAFS) oscillations ($k^2\chi(k)$), as shown in Figure 3g. The existence of characteristic peaks at 6.8, 8.1, and 9.2 $Å^{-1}$ are indicative of a layered structure, while the single, sharp profiles of the latter two oscillations confirm the hexagonal symmetry of the [MnO_6] layers [32, 36]. The k-space oscillation profiles of all samples exhibited a high degree of resemblance in both phase and amplitude, indicating that the overall configuration was preserved after ion intercalation[39].

The corresponding Fourier-transform (FT) EXAFS analysis (Figure 3h and Figure S9) provides insights into local structural changes. In the 1–4 Å range of Mn k^2-weight FT-EXAFS spectra, two dominant peaks at approximately 1.50 Å and 2.50 Å originate from the Mn–O scattering path within the [MnO_6] octahedra and the edge-sharing Mn–Mn path within the layers, respectively [32, 38]. Quantitative fitting reveals that ion intercalation shortens the Mn–O bond length (from 1.96 ± 0.03 Å in Birnessite to 1.82 ± 0.06 Å in MgBir, Table S2) while increasing the Mn–Mn distance (from 2.95 ± 0.01 Å to 3.06 ± 0.05 Å). Furthermore, the attenuation of the Mn–O peak intensity in the intercalated samples suggests a decrease in the coordination number of oxygen around Mn, pointing to an increase in oxygen vacancies [35]. The R-space fitting results further support this conclusion. The Wavelet Transform (WT) contour plots (Figure 3i) offer a visualized comparison of the Mn coordination environments across the samples. Taken together, the XPS and XAS analyses demonstrate that covalency regulation of Mn–O induces a synergistic remodeling of both the electronic structure and the local atomic coordination.

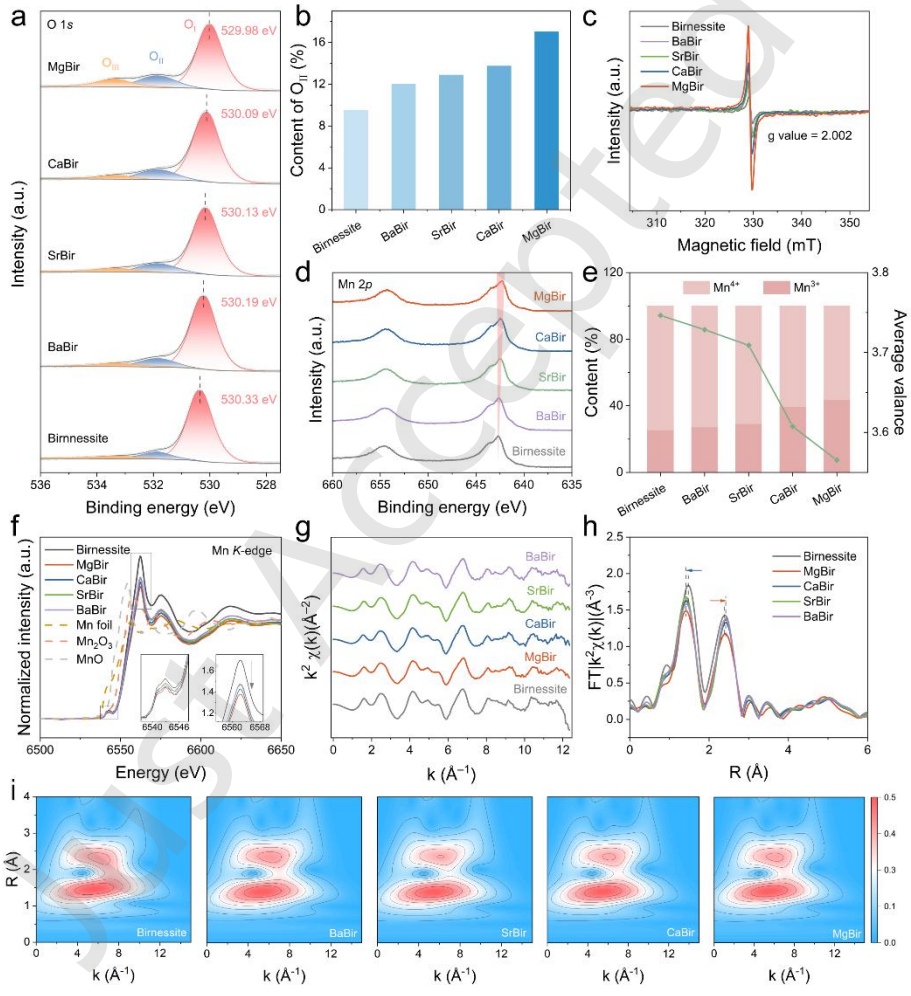


Figure 3. Electronic state and coordination structure analysis. (a) High-resolution XPS spectra of various samples for O 1*s* and (b) Percentage content of oxygen vacancy (O_{II}) in the corresponding samples. (c) EPR spectra of various samples. (d) High-resolution XPS spectra of various samples for Mn 2*p* and (e) Percentage contents of Mn^{3+}, Mn^{4+} and the average valence of Mn element. (f) Normalized Mn *K*-edge XANES spectra of various samples and the corresponding reference samples (Inset: the magnified adsorption edge). Spectra of k^2-weighted EXAFS in (g) K-space and corresponding Fourier transformed magnitude in (h) R-space of various samples. (i) Wavelet transforms of the experimental k^2-weight EXAFS spectra.

2.4 Investigations of OXD-like performance and kinetics

The OXD-like activities of the pristine and ion-intercalated Birnessite were evaluated by a typical chromogenic reaction, where 3,3′,5,5′-tetramethylbenzidine (TMB) acted as an electron donor for the O_2 reduction process [34]. The catalytic oxidation of TMB was monitored by tracking the characteristic absorbance at 652 nm (Figure 4a). A negligible signal was observed for the TMB-only control, whereas the pristine Birnessite showed a markedly higher absorbance, confirming its intrinsic OXD-like property [13]. Remarkably, the intercalation of catalytically inert alkaline-earth metal ions significantly enhanced this activity (Figure 4b). The catalytic efficacy aligns with the increased Mn–O covalency, linking the catalytic enhancement to the electronic structure modulation directly.

We conducted steady-state kinetic assays and specific activity (SA) measurements to compare the catalytic performance of

various catalysts (Figure 4c-d) [12, 40]. As shown in Figure 4e, the SA value of MgBir (17.6 U mg^{-1}) is 2.4 times higher than that of pristine Birnessite (7.4 U mg^{-1}). Plotting the initial reaction rate and substrate concentration, a series of typical Michaelis-Menten curves and corresponding Lineweaver–Burk double reciprocal plots (Figure S10) were obtained [40]. The calculated maximum reaction rate (V_{max}) value (Figure 4f and Table S3) of Birnessite, BaBir, SrBir, CaBir, and MgBir were 197.86, 251.18, 268.23, 277.25 and 344.84 μmol min^{-1}, respectively, indicating enhanced catalytic efficiency. Concurrently, the Michaelis constant (K_m) of MgBir (0.88 mM) is significantly lower than that of Birnessite (1.47 mM), reflecting a strengthened substrate affinity. Given the normalization to active sites, the superior performance of the ion-intercalated samples is unambiguously attributed to the elevated electron density within the Mn–O bond resulting from enhanced covalency.

To elucidate the catalytic mechanism, EPR test and reactive oxygen species (ROS) trapping experiments were conducted. The 2,2,6,6-tetramethylpiperidine (TEMP) and 5,5-dimethyl-1-pyrroline N-oxide (DMPO) were used as spin-capture agents for the ROS detection [41]. As shown in Figure 4g, two characteristic EPR spectra with the relative signal intensity of 1:1:1:1 and 1:1:1 were observed, indicating the presence of $O_2^{\bullet-}$ and $^1O_2$ during the catalytic process [17, 42]. The absence of the 1:2:2:1 signature for $^{\bullet}OH$ indicates its negligible generation. Furthermore, ROS scavenging experiment was conducted to provide additional evidence (Figure 4h and Figure S11), in which n-Butanol, Tryptophan (Trp) and 1,4-Benzoquinone (p-BQ) were used as the scavenger to track $^{\bullet}OH$, $^1O_2$, and $O_2^{\bullet-}$, the absorbance decrease at 652 nm indicating the production of c and $^1O_2$ [12]. The UV-vis spectra obtained under different gas conditions (Figure S12) demonstrate the involvement of dissolved oxygen in the OXD-like process [13]. Collectively, these results demonstrate that the catalyst activates molecular oxygen through an electron transfer process, which generates ROS that mediate the oxidation of substrates via an OXD-like pathway.

The catalysts' practical applicability was assessed by evaluating their performance under diverse conditions, including pH, temperature, chemical stability, and storage duration (Figure S13 and Figure S14). The nanozymes show peak performance in weakly acidic medium (pH 4). Within the temperature range of 4–70 °C, increasing the incubation temperature slightly accelerated the reaction kinetics. Excellent chemical stability was evidenced by the retention of over 90% initial activity after treatment in 0.1 M HCl (pH ≈ 1) or 1 M NaOH (pH ≈ 14) for 24h [34]. Moreover, negligible activity loss (<5%) was observed after 20 days of storage, highlighting outstanding long-term stability. Finally, a comparative analysis with previously reported nanozymes confirms that both the pristine and ion-intercalated Birnessite samples exhibit highly competitive, if not superior, OXD-like kinetics (Figure 4i, Table S4), underscoring the effectiveness of our covalency-regulation strategy.

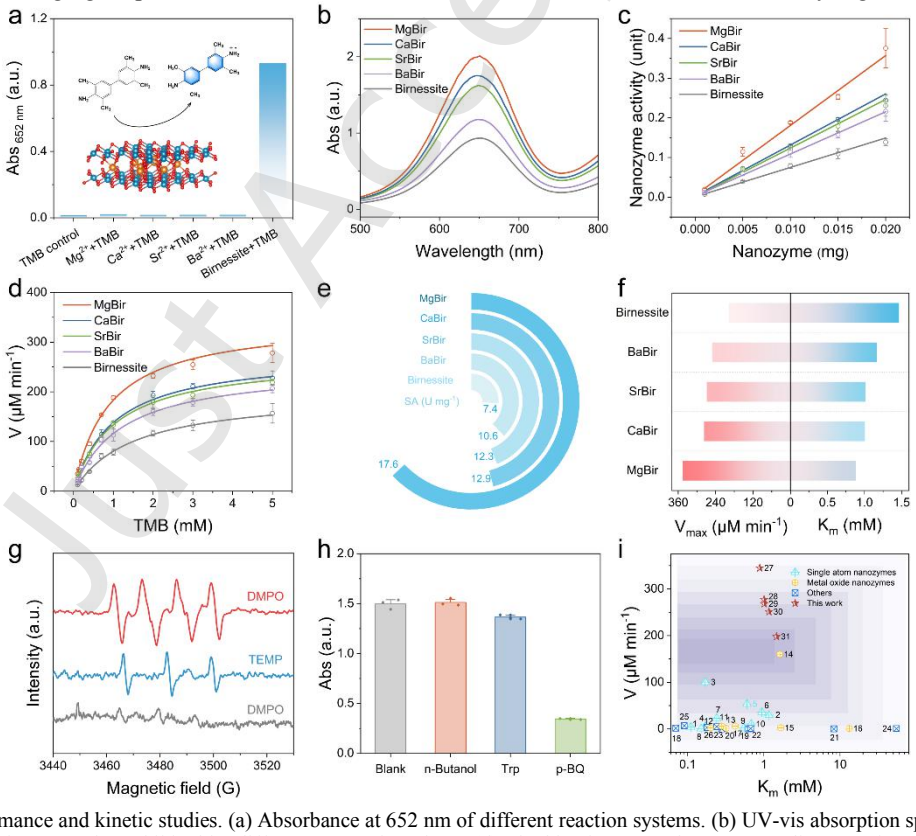


Figure 4. OXD-like performance and kinetic studies. (a) Absorbance at 652 nm of different reaction systems. (b) UV-vis absorption spectra of catalytic systems. (c) Catalytic activity of various samples exhibited by different mass of catalysts. (d) The kinetic curves the corresponding samples. Comparison of (e) Specific activity (U mg^{-1}) and (f) Kinetics parameter between various samples. The generation of reactive oxygen species detected by (g) EPR and (h) Scavengers (n-Butanol, Trp and p-BQ). (i) The comparison of the kinetics parameter in diverse nanozymes.

2.5 Mechanistic insights from DFT calculations

To elucidate the origin of the enhanced OXD-like activity induced by intercalated cations, we performed a series of DFT calculations to examine the reaction pathway. Based on XPS and XAS results, structural models of the catalysts were constructed with layered [MnO_6] edge-sharing octahedra, incorporating intercalated cations (Mg^{2+}, Ca^{2+}, Sr^{2+}, Ba^{2+}) and the corresponding oxygen vacancies. For the overall OXD-like

Just Accepted

catalytic cycle, sufficient adsorption of O_2 or TMB, electron transfer from substrates, and catalytic center regeneration are three essential steps [12, 17]. As the initial step, substrate adsorption critically influences subsequent electron transfer from the substrate to adsorbed intermediates. Projected density of states (PDOS) calculations for Mn 3*d* and O 2*p* orbitals after O_2 adsorption were conducted to analyze electronic interactions (Figure 5a and Figure S15). Relative to pristine Birnessite, in MgBir with strong Mn–O covalency, the upward shift of the Mn 3*d* band results in more antibonding orbitals migrating above the Fermi level. This reduces electron occupation in the antibonding orbitals, thereby enhancing the bonding interaction with adsorbed O_2 ($*O_2$) (Figure 5b) [29]. Analogously, the higher energy of the $*O_2$ antibonding orbital implies lower antibonding occupancy and a stronger chemical bond. Moreover, a larger overlap between Mn 3*d* and O 2*p* orbitals signifies strengthened interaction between Mn sites and adsorbed $*O_2$, which facilitates interfacial electron transfer [12, 43]. This interpretation is corroborated by the calculated adsorption energies (Figure 5c and Figure S16), The adsorption energies of O_2 on MgBir (−1.75 eV) is much larger than that on Birnessite (−0.03 eV). In line with the TMB-adsorption-initiated mechanism proposed by Wu et al., we also computed the adsorption energies of TMB on oxygen sites [44-45]. The increased adsorption energy in MgBir (−1.26 eV) indicates more efficient TMB adsorption, which can be ascribed to the elevated O 2*p*-band center resulting from enhanced Mn–O covalency [46]. After ions intercalation, the stronger adsorption of both O_2 and TMB implies superior substrate affinity, which is consistent with the experimental Michaelis constant (K_m) results.

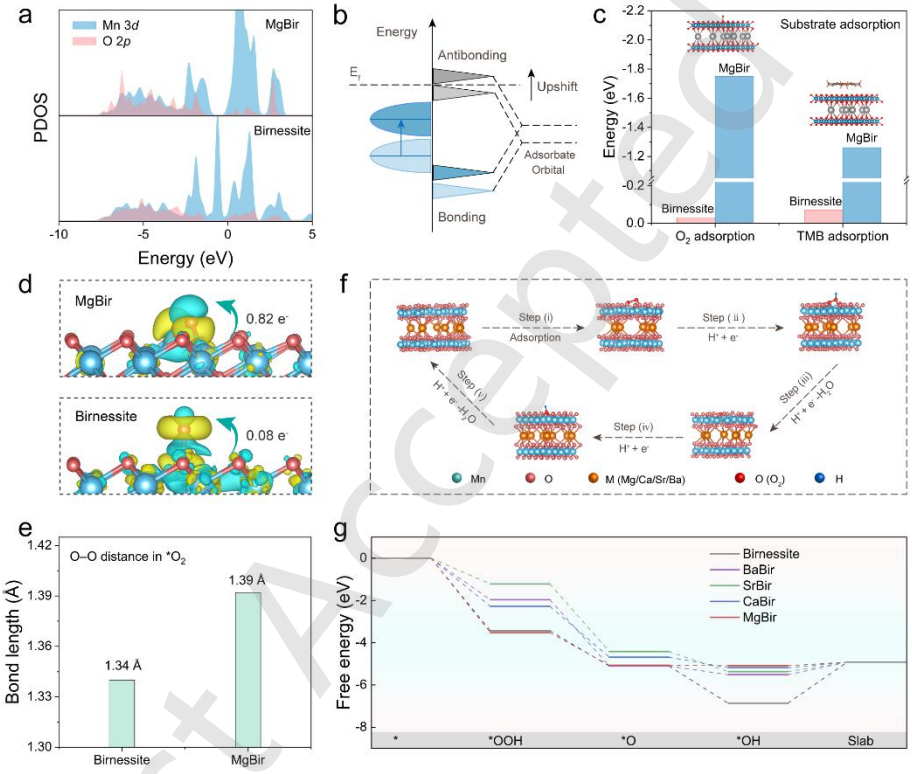


Figure 5. Mechanistic insights from DFT calculations. (a) PDOS of Mn 3*d* and O 2*p* orbitals and (b) Schematic illustration of the effect of *d*-band position on O_2 adsorption. (c) Calculated O_2 adsorption energies and TMB absorption energies. (d) Charge density difference of O_2 adsorbed on various samples (yellow and green contours denoted the accrual and expenditure of electrons, respectively). (e) The calculated O–O bond length in adsorbed O_2. (f) Corresponding proposed reaction pathways of O_2 reduction with optimized adsorption configurations. (g) Gibbs free energy change profiles for OXD-like reaction of various samples with adsorbed intermediates.

We next investigated the electron transfer process during the OXD-like reaction. Charge density difference and Bader charge analyses were performed to probe the interfacial electron transfer between the active site and the substrate (Figure 5d and Figure S17). After the adsorption of O_2, more interfacial electrons accumulate on the $*O_2$ adsorbate bound to Mn atoms compared with that of Birnessite. Specifically, $*O_2$ obtains 0.82 e^- and 0.08 e^- from MgBir and Birnessite, respectively, indicating a large amount of charge transfer [25, 47]. We posit that efficient electron transfer facilitates thorough O_2 activation. To verify this, the O–O bond length in adsorbed O_2 was examined (Figure 5e and Figure S18). The calculated O–O distance increases from 1.34 Å in Birnessite to 1.39 Å in MgBir, reflecting significant bond elongation and weakening. This weakening is attributed to electron transfer from Mn atoms populating the O_2 antibonding orbitals, a process enhanced by the upshifted Mn 3*d*-band center resulting from strengthened covalency [48]. Thus, the strong absorption promotes the charge transfer from Mn site to adsorbed O_2 and O─O bond was weakened.

The catalytic pathway and corresponding free energy profiles for the OXD-like reaction were systematically computed (Figure 5f and Figure 5g; Table S5) [34, 49]. As established in prior studies, the catalytic cycle involves four proton-coupled electron transfer steps: (i) the adsorption of an O_2 molecule on the Mn center and then hydrogenated to form *OOH intermediate, (ii) *O and one molecule H_2O production, (iii) the formation of *OH and (iv) the other molecule H_2O desorption with concomitant catalytic center regeneration [44]. The free energy profiles reveal that steps (i) to (iii) are spontaneous ($\Delta G < 0$), whereas H_2O desorption in step (iv) constitutes the rate-determining step (RDS) [15]. Pristine Birnessite exhibits strong *OH adsorption, impeding H_2O desorption and resulting in a

Just Accepted

high free energy change of 1.947 eV in step (iv). In contrast, ion intercalation significantly reduces the H_2O desorption energy to 0.597 eV (BaBir), 0.450 eV (SrBir), 0.260 eV (CaBir), and 0.170 eV (MgBir). This lower activation barrier underscores the efficacy of covalency modulation and rationalizes the experimentally observed increase in V_{max}. In conclusion, DFT calculations unequivocally demonstrate that the electronic modulation of Mn and O sites induced by intercalated cations is the fundamental origin of the superior OXD-like activity.

2.6 Colorimetric sensing platform for antioxidants detection

Based on the superior OXD-like activities observed, a colorimetric sensor array was constructed using Birnessite, SrBir, and MgBir as sensing elements for the discrimination of various antioxidants, including tannic acid (TA), L-Ascorbic acid (AA), (-)-Epigallocatechin (EGC), gallic acid (GA) and L-Cysteine (CYS). In this system, the colorimetric signal arises from the oxidation of TMB (TMBox) catalyzed by the OXD-like activity of the materials [50]. In the presence of different antioxidants, distinct response patterns are generated due to their varying reducing capacities toward TMBox, leading to differential inhibition of the catalytic activity [51]. By integrating linear discriminant analysis (LDA) and hierarchical cluster analysis (HCA), the antioxidants could be accurately identified.

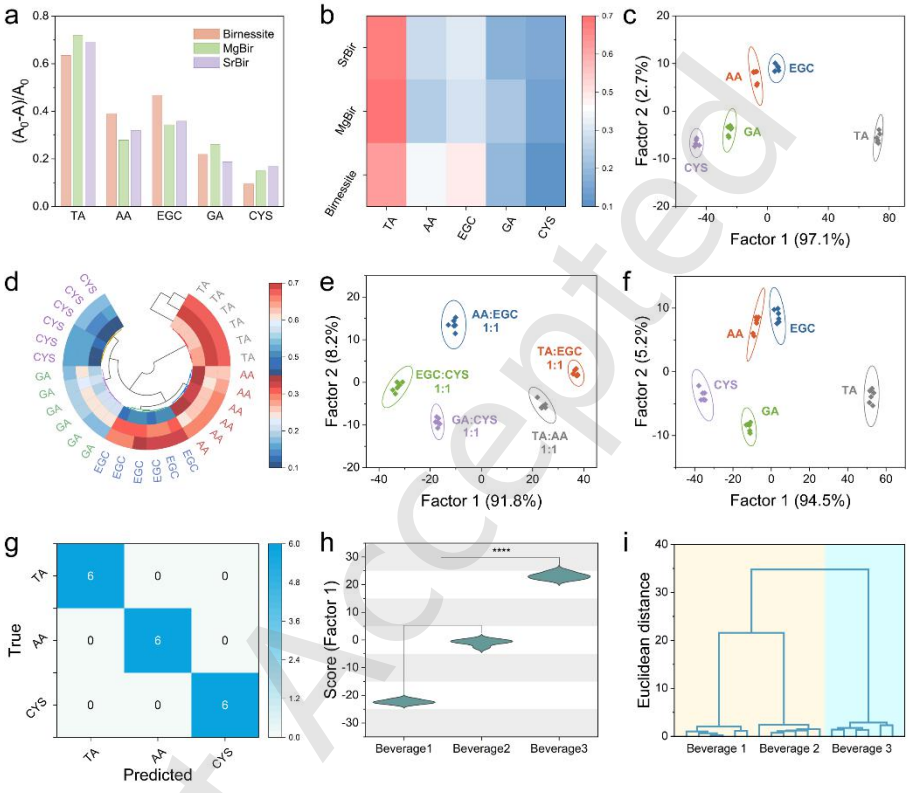


Figure 6. (a) Colorimetric response fingerprint diagram, (b) Corresponding heat map, (c) LDA score plot and (d) Circular clustered heatmap of this sensor array toward five antioxidants (28 μmol L^{-1}). (e) The binary mixture with a total concentration of 28 μmol L^{-1}. (f) Anti-interference assay for sensor array toward 7 interferences. (g) Confusion matrix. (h) Plot of the factor 1 and (i) HCA plot for the three beverage samples.

The discrimination capability of the sensor array was first evaluated at a concentration of 28 μmol L^{-1}. To quantify the inhibitory effect of each antioxidant on the sensor components, the absorbance at 652 nm was recorded and normalized as $(A_0\text{-}A)/A_0$ (A and A_0 represent the absorbance in the presence and absence of an antioxidant, respectively) [51]. A 3×5×6 data (3 component, 5 antioxidants, 6 replicates) matrix was obtained consequently. As shown in Figure 6a, each antioxidant elicits a unique fingerprint-like response pattern across the three sensors. Furthermore, the heatmap analysis (Figure 6b) reveals that different degrees of catalytic inhibition are contributed by various antioxidants, demonstrating the feasibility of discriminating all five species. The response matrix was then analyzed using LDA and two discriminant factors were used to project the training data into a two-dimensional canonical score plot. As displayed in Figure 6c, the six replicates of each antioxidant form well-separated clusters with non-overlapping 95% confidence regions. This confirms that the sensor array can clearly distinguish five antioxidants at the same concentration. Additionally, 30 groups of data (5 antioxidants × 6 replicates) could be gradually divided into five clusters in HCA analysis (Figure 6d), which also confirms the LDA result [50]. The sensor array also maintained robust discrimination across a range of concentrations (Figure S19). Quantitative experiments were conducted to assess the sensor's performance across different concentrations (6–50 μmol L^{-1}, Figure S20). The results show that TA, AA, EGC, GA, and CYS can be effectively discriminated in this range, with discriminant factor 1 exhibiting a linear relationship with either the concentration or the logarithm of concentration for each antioxidant.

To evaluate performance under more complex conditions, the sensor was challenged with binary and ternary antioxidant mixtures. LDA and HDA results confirmed that different mixture combinations could be clearly distinguished without misclassification (Figure 6e and Figure S21). Potential interferents were introduced into the system, such as sodium chloride, potassium chloride, natural β-carotene, glycine, lysine, glucose, and trisodium citrate dihydrate, the result showed that the sensor array possessed powerful anti-interference capability

Just Accepted

(Figure 6f and Figure S22). A confusion matrix was constructed to evaluate classification accuracy (Figure 6g). The complete agreement between predicted and actual labels demonstrates the high precision of the sensor in identifying both antioxidant type and concentration [52]. To assess practical utility, the array was applied to the analysis of real beverage samples (Figure S23). The violin plots revealed a clear distinction in discriminant factor 1 scores among the different beverage samples (Figure 6h). All three types of beverages were accurately classified (Figure 6i), underscoring the potential of this platform for rapid and reliable antioxidant level assessment [51].

3 Conclusions

In summary, an ion intercalation strategy is proposed to probe the influence of M–O covalency on OXD-like activity and reveal the mechanism in metal oxide nanozymes. The polarization effect induced by intercalated ions strengthens the intralayer Mn–O covalency in Birnessite, which in turn increases the electron density at both Mn and O sites and upshifts their respective band centers (Mn 3*d* and O 2*p*), leading to a synergistic optimization of the electronic and band structures. Theoretical calculations corroborate that this enhanced covalency promotes substrate (TMB and O_2) adsorption, facilitates electron transfer, weakens the O–O bond to trigger oxygen dissociation, and lowers the energy barrier of the rate-determining step. Leveraging the superior OXD-like activity, a colorimetric sensor array was constructed for the identification and quantitative analysis of five antioxidants (TA, AA, EGC, GA, CYS). This work elucidates the fundamental mechanism of Mn–O covalency in regulating nanozyme activity and establishes a novel paradigm for the electronic-structure engineering of metal oxide-based nanozymes.

Electronic Supplementary Material: Supplementary material (Experimental details, DFT calculations, FT-IR, XPS, BET, XAS, DRT, and other supplementary characterizations, as well as additional UV-vis tests.) is available in the online version of this article at https://doi.org/10.26599/NR.2026.94909224.

Data availability

All data needed to support the conclusions in the paper are presented in the manuscript and/or the Electronic Supplementary Material. Additional data related to this paper may be requested from the corresponding author upon request.

Acknowledgements

This work was supported by the National Natural Science Foundation of China (22393930, 22034006 and 22202080), the National Key Research and Development Program of China (2022YFF0710000) and the Jilin talent Development Foundation (E41S2001).

Declaration of competing interest

All the contributing author(s) report(s) no conflict of interests in this work.

Author contribution statement

Yao-Yao Chen: Conceptualization, data curation, formal analysis, investigation, methodology, software, writing-original draft, writing-review & editing. Bo-Han Yao: Conceptualization, methodology, writing-review & editing. Qi-Lin Zhao: Formal analysis, investigation, methodology. Li-Min Ma: Methodology, data curation, writing-review & editing. Rui Han: Writing-review & editing, data curation. Dong-Ming Xu: Writing-review & editing, data curation. Chun-Xia Ma: Writing-review & editing. Bing Zhang: Writing-review & editing. Zhi-Ying Jin: Writing-review & editing. Dong-Xu Jiao: Methodology, resources, validation. Huan-Huan Xing: Methodology, resources, software. De-Wen Wang: Conceptualization, data curation, formal analysis, funding acquisition, methodology, project administration, resources, supervision, writing-review & editing. Xiu-Rong Yang: Conceptualization, data curation, formal analysis, funding acquisition, methodology, project administration, resources, supervision, writing-review & editing. All the authors have approved the final manuscript."

Informed consent

Not applicable.

Ethics statement

Not applicable.

Use of AI statement

None.

References

[1] Wei, H.; Wang, E. K. Nanomaterials with enzyme-like characteristics (nanozymes): Next-generation artificial enzymes. *Chem. Soc. Rev.* **2013**, *42*, 6060-6093.

[2] Wu, J. J. X.; Wang, X. Y.; Wang, Q.; Lou, Z. P.; Li, S. R.; Zhu, Y. Y.; Qin, L.; Wei, H. Nanomaterials with enzyme-like characteristics (nanozymes): Next-generation artificial enzymes (ii). *Chem. Soc. Rev.* **2019**, *48*, 1004-1076.

[3] Zhang, R. F.; Yan, X. Y.; Fan, K. L. Nanozymes inspired by natural enzymes. *Acc. Mater. Res.* **2021**, *2*, 534-547.

[4] Ji, S. F.; Jiang, B.; Hao, H. G.; Chen, Y. J.; Dong, J. C.; Mao, Y.; Zhang, Z. D.; Gao, R.; Chen, W. X.; Zhang, R. F.; Liang, Q.; Li, H. J.; Liu, S. H.; Wang, Y.; Zhang, Q. H.; Gu, L.; Duan, D. M.; Liang, M. M.; Wang, D. S.; Yan, X. Y.; Li, Y. D. Matching the kinetics of natural enzymes with a single-atom iron nanozyme. *Nat. Catal.* **2021**, *4*, 407-417.

[5] Gao, L. Z.; Zhuang, J.; Nie, L.; Zhang, J. B.; Zhang, Y.; Gu, N.; Wang, T. H.; Feng, J.; Yang, D. L.; Perrett, S.; Yan, X. Y. Intrinsic peroxidase-like activity of ferromagnetic nanoparticles. *Nat. Nanotechnol.* **2007**, *2*, 577-583.

[6] Liu, Q. W.; Zhang, A. M.; Wang, R. H.; Zhang, Q.; Cui, D. X. A review on metal- and metal oxide-based nanozymes: Properties, mechanisms, and applications. *Nano-Micro Lett.* **2021**, *13*, 154.

[7] Liu, C.; Gui, L.; Zheng, J. J.; Xu, Y. Q.; Song, B. L.; Yi, L.; Jia, Y. J.; Taledaohan, A.; Wang, Y. J.; Gao, X. F.; Qiao, Z. Y.; Wang, H.; Tang, Z. Y. Intrinsic strain-mediated ultrathin ceria nanoantioxidant. *J. Am. Chem. Soc.* **2023**, *145*, 19086-19097.

[8] Luo, W. J.; Zhu, C. F.; Su, S.; Li, D.; He, Y.; Huang, Q.; Fan, C. H. Self-catalyzed, self-limiting growth of glucose oxidase-mimicking gold nanoparticles. *ACS Nano* **2010**, *4*, 7451-7458.

[9] Ghosh, S.; Roy, P.; Karmodak, N.; Jemmis, E. D.; Mugesh, G. A redox modulatory Mn_3O_4 nanozyme with multi-enzyme activity provides efficient cytoprotection to human cells in a parkinson's disease model. *Angew. Chem., Int. Ed.* **2017**, *56*, 14267-14271.

[10] Fan, H. Z.; Zheng, J. J.; Xie, J. Y.; Liu, J. W.; Gao, X. F.; Yan, X. Y.; Fan, K. L.; Gao, L. Z. Surface ligand engineering ruthenium nanozyme superior to horseradish peroxidase for enhanced immunoassay. *Adv. Mater.* **2024**, *36*, 2300387.

[11] Zhang, Z. J.; Zhang, X. H.; Liu, B. W.; Liu, J. W. Molecular imprinting on inorganic nanozymes for hundred-fold enzyme specificity. *J. Am. Chem. Soc.* **2017**, *139*, 5412-5419.

[12] Cai, Y. J.; Wu, Y.; Tang, Y. J.; Xu, W. Q.; Chen, Y. F.; Su, R. N.; Fan, Y. X.; Jiang, W. X.; Wen, Y. T.; Gu, W. L.; Sun, H. C.; Zhu, C. Z. In

Just Accepted

situ defect engineering of Fe-MIL for self-enhanced peroxidase-like activity. *Small* **2024**, *20*, 2403354.

[13] Wang, Y.; Cho, A.; Jia, G. R.; Cui, X. Q.; Shin, J.; Nam, I.; Noh, K.-J.; Park, B. J.; Huang, R.; Han, J. W. Tuning local coordination environments of manganese single-atom nanozymes with multi-enzyme properties for selective colorimetric biosensing. *Angew. Chem., Int. Ed.* **2023**, *62*, e202300119.

[14] Ma, L. M.; Wang, Y.; Chen, Y. Y.; Han, R.; Xu, D. M.; Jiao, D. X.; Wang, D. W.; Yang, X. R. Construction of frustrated lewis pairs for efficient artificial enzyme. *Adv. Funct. Mater.* **2025**, *35*, 2503358.

[15] Zhang, Y. M.; Kang, Y. Q.; Wei, X. Q.; Chen, C. J.; Zhai, Y. L.; Zhu, C. Z.; Jiao, L.; Lu, X. Q.; Yamauchi, Y. Modulating p-d orbital hybridization in mesoporous medium-entropy alloy nanozymes with enhanced peroxidase-like activity. *ACS Nano* **2025**, *19*, 24013-24022.

[16] Zhang, K.; Li, N. N.; Weng, Y. L.; Kang, Y. B.; Lee, J. Y.; Zhang, H. F.; Ding, Y. H.; Han, X. T.; Pang, H. Navigating covalency of cobalt oxides for enhanced oxygen evolution. *Adv. Funct. Mater.* **2025**, *35*, 2507212.

[17] Wang, Y.; Paidi, V. K.; Wang, W. Z.; Wang, Y.; Jia, G. R.; Yan, T. Y.; Cui, X. Q.; Cai, S. H.; Zhao, J. X.; Lee, K. S.; Lee, L. Y. S.; Wong, K. Y. Spatial engineering of single-atom Fe adjacent to Cu-assisted nanozymes for biomimetic O_2 activation. *Nat. Commun.* **2024**, *15*, 2239.

[18] Xu, G. Z.; Zhou, H.; Ma, D. R.; Huang, J. H.; Zhang, R. M.; Chen, Y.; Tang, Z. Y.; Yu, H. Y.; Li, W. W.; Xia, D. H. Tailoring covalency competition of spinel oxides to enhance the reactivity of surface atomic oxygen for boosted catalytic ozonation. *Appl. Catal., B* **2026**, *381*, 125905.

[19] Yang, Y.; Chen, Y. T.; Yan, Y. Y.; Yao, B. H.; Xing, H. H.; Jiao, D. X.; Xing, Z. C.; Wang, D. W.; Yang, X. R. Metal-oxygen octahedra regulation of iridium-based perovskites for efficient and durable acidic water oxidation. *Adv. Funct. Mater.* **2025**, *35*, 2506467.

[20] Zhou, Y.; Sun, S. N.; Song, J. J.; Xi, S. B.; Chen, B.; Du, Y. H.; Fisher, A. C.; Cheng, F. Y.; Wang, X.; Zhang, H.; Xu, Z. J. Enlarged Co–O covalency in octahedral sites leading to highly efficient spinel oxides for oxygen evolution reaction. *Adv. Mater.* **2018**, *30*, 1802912.

[21] Li, C.; Ye, B. R.; Ouyang, B.; Zhang, T. F.; Tang, T.; Qiu, Z.; Li, S. P.; Li, Y. Q.; Chen, R. H.; Wen, W.; Song, M.; Mei, B. B.; Xia, X. H.; Zhang, Y. Q. Dual doping of N and F on Co_3O_4 to activate the lattice oxygen for efficient and robust oxygen evolution reaction. *Adv. Mater.* **2025**, *37*, 2501381.

[22] Thenuwara, A. C.; Cerkez, E. B.; Shumlas, S. L.; Attanayake, N. H.; McKendry, I. G.; Frazer, L.; Borguet, E.; Kang, Q.; Remsing, R. C.; Klein, M. L.; Zdilla, M. J.; Strongin, D. R. Nickel confined in the interlayer region of birnessite: An active electrocatalyst for water oxidation. *Angew. Chem., Int. Ed.* **2016**, *55*, 10381-10385.

[23] Lu, H. B.; Zhang, W. F.; Tao, L.; Liu, F.; Zhang, J. Enhanced removal of antimony by acid birnessite with doped iron ions: Companied by the structural transformation. *Chemosphere* **2019**, *226*, 834-840.

[24] Yang, J. L.; Zhang, Y.; Ge, Y. Z.; Tang, S.; Li, J.; Zhang, H.; Shi, X. D.; Wang, Z. T.; Tian, X. L. Interlayer engineering of layered materials for efficient ion separation and storage. *Adv. Mater.* **2024**, *36*, 2311141.

[25] Si, H. B.; Du, D. X.; Jiao, C. C.; Sun, Y.; Li, L.; Tang, B. Biomimetic synergistic effect of redox site and lewis acid for construction of efficient artificial enzyme. *Nat. Commun.* **2024**, *15*, 6315.

[26] Yin, Z. H.; Huang, Y.; Song, K. P.; Li, T. T.; Cui, J. Y.; Meng, C.; Zhang, H. G.; Wang, J. J. Ir single atoms boost metal–oxygen covalency on selenide-derived NiOOH for direct intramolecular oxygen coupling. *J. Am. Chem. Soc.* **2024**, *146*, 6846-6855.

[27] Wang, L. Q.; Hung, S. F.; Zhao, S.; Wang, Y.; Bi, S. W.; Li, S. X.; Ma, J. J.; Zhang, C. C.; Zhang, Y.; Li, L. L.; Chen, T. Y.; Chen, H. Y.; Hu, F.; Wu, Y. P.; Peng, S. J. Modulating the covalency of Ru-O bonds by dynamic reconstruction for efficient acidic oxygen evolution. *Nat. Commun.* **2025**, *16*, 3502.

[28] Yu, Z. Y.; Duan, Y.; Kong, Y.; Zhang, X. L.; Feng, X. Y.; Chen, Y.; Wang, H. J.; Yu, X. X.; Ma, T.; Zheng, X. S.; Zhu, J. F.; Gao, M. R.; Yu, S. H. General synthesis of tube-like nanostructured perovskite oxides with tunable transition metal–oxygen covalency for efficient water electrooxidation in neutral media. *J. Am. Chem. Soc.* **2022**, *144*, 13163-13173.

[29] Wang, S. L.; Ju, Z. J.; Wang, Y. W.; Liu, Z. J.; Wang, X. Z.; Jiao, H.; Cao, M. H.; Wang, Y. D.; Yin, W. Y.; Zhao, Y. L. Synergizing Pt–O–Mo coupling and electron gradient: A nanozyme paradigm for low-dose tumor radiosensitization. *ACS Nano* **2026**, *20*, 11254-11273.

[30] McKenzie, R. M. The synthesis of birnessite, cryptomelane, and some other oxides and hydroxides of manganese. *Mineral. Mag.* **1971**, *38*, 493-502.

[31] Yin, H.; Tan, W. F.; Zheng, L. R.; Cui, H. J.; Qiu, G. H.; Liu, F.; Feng, X. H. Characterization of Ni-rich hexagonal birnessite and its geochemical effects on aqueous Pb^{2+}/Zn^{2+} and As(iii). *Geochim. Cosmochim. Acta* **2012**, *93*, 47-62.

[32] Ding, J. Y.; Du, H. L.; Cai, G. H.; Huang, S. Z.; Peng, C. Y.; Wang, L. L.; Luo, J. R.; Wang, X. S.; Xue, M. Q.; Zhang, X. X.; Sun, J. L.; Chen, J. T. Layer symmetry and interlayer engineering of birnessites towards high-performance rechargeable aqueous Zn-MnO_2 batteries. *Nano Energy* **2023**, *112*, 108485.

[33] Yin, H.; Liu, F.; Feng, X. H.; Liu, M. M.; Tan, W. F.; Qiu, G. H. Co^{2+}-exchange mechanism of birnessite and its application for the removal of Pb^{2+} and As(iii). *J. Hazard. Mater.* **2011**, *196*, 318-326.

[34] Chen, D.; Xia, Z. M.; Guo, Z. X.; Gou, W. Y.; Zhao, J. L.; Zhou, X. M.; Tan, X. H.; Li, W. B.; Zhao, S. J.; Tian, Z. M.; Qu, Y. Q. Bioinspired porous three-coordinated single-atom Fe nanozyme with oxidase-like activity for tumor visual identification via glutathione. *Nat. Commun.* **2023**, *14*, 7127.

[35] Wang, F. Q.; Feng, L.; Zhang, M. W.; Cong, H. L. Engineering oxygen nonbonding states in high entropy hydroxides for scalable water oxidation. *Nat. Commun.* **2025**, *16*, 6624.

[36] Lv, G. C.; Xing, X. B.; Liao, L. B.; An, P. F.; Yin, H.; Mei, L. F.; Li, Z. H. Synthesis of birnessite with adjustable electron spin magnetic moments for the degradation of tetracycline under microwave induction. *Chem. Eng. J.* **2017**, *326*, 329-338.

[37] Saratovsky, I.; Wightman, P. G.; Pastén, P. A.; Gaillard, J.-F.; Poeppelmeier, K. R. Manganese oxides: parallels between abiotic and biotic structures. *J. Am. Chem. Soc.* **2006**, *128*, 11188-11198.

[38] Su, H.; Yang, C. Y.; Liu, M. H.; Zhang, X.; Zhou, W. L.; Zhang, Y. H.; Zheng, K.; Lian, S. X.; Liu, Q. H. Tensile straining of iridium sites in manganese oxides for proton-exchange membrane water electrolysers. *Nat. Commun.* **2024**, *15*, 95.

[39] Yao, B. H.; Chen, Y. T.; Yan, Y. Y.; Yang, Y.; Xing, H. H.; Xu, Y. C.; Jiao, D. X.; Xing, Z. C.; Wang, D. W.; Yang, X. R. Iron-induced localized oxide path mechanism enables efficient and stable water oxidation. *Angew. Chem., Int. Ed.* **2025**, *64*, e202416141.

[40] Zheng, J. J.; Zhu, F. Y.; Song, N. N.; Deng, F.; Chen, Q.; Chen, C.; He, J. Y.; Gao, X. F.; Liang, M. M. Optimizing the standardized assays for determining the catalytic activity and kinetics of peroxidase-like nanozymes. *Nat. Protoc.* **2024**, *19*, 3470-3488.

[41] Ye, J.; Li, C. S.; Xu, J. T.; Liu, S.; Qu, J. W.; Wang, Q.; Cao, J.; Zhao, Y. Y.; Li, C. R.; Yang, P. P. Engineered nanozymes with asymmetric Mn─O─Ce sites for intratumorally leveraged multimode therapy. *Adv. Mater.* **2025**, *37*, 2419673.

[42] Zhu, Y.; Wang, W. Y.; Cheng, J. J.; Qu, Y. T.; Dai, Y.; Liu, M. M.; Yu, J. N.; Wang, C. M.; Wang, H. J.; Wang, S. C.; Zhao, C.; Wu, Y. E.; Liu, Y. Z. Stimuli-responsive manganese single-atom nanozyme for tumor therapy via integrated cascade reactions. *Angew. Chem., Int. Ed.* **2021**, *60*, 9480-9488.

[43] Hao, L.; Liang, X. J.; Zhang, Y. W.; Zhang, Z. J.; Han, Y.; Jin, Y.; Li, L. W.; Magrini, A.; Bottini, M.; Gao, S. T.; Zhang, J. C. Fine-tuning the d-band center position of zinc to increase the anti-tumor activity of single-atom nanozymes. *Adv. Mater.* **2024**, *36*, 2412368.

[44] Wu, J. J. X.; Wang, Z. Z.; Jin, X.; Zhang, S.; Li, T.; Zhang, Y. H.; Xing, H.; Yu, Y.; Zhang, H. G.; Gao, X. F.; Wei, H. Hammett relationship in oxidase-mimicking metal–organic frameworks revealed through a protein-engineering-inspired strategy. *Adv. Mater.* **2021**, *33*, 2005024.

[45] Shen, X. M.; Wang, Z. Z.; Gao, X. J. J.; Gao, X. F. Reaction mechanisms and kinetics of nanozymes: Insights from theory and computation. *Adv. Mater.* **2024**, *36*, 2211151.

[46] Ma, L. M.; Wang, Y.; Chen, Y. Y.; Xu, D. M.; Han, R.; Jiao, D.

Just Accepted

X.; Xing, H. H.; Wang, D. W.; Yang, X. R. Optimizing the electronic structure of iron oxides via nonmetallic dopants for enhanced peroxidase mimetic catalysis. *ACS Nano* **2025**, *19*, 28410-28421.

[47] Yu, Z. C.; Xu, Z. J.; Zeng, R. J.; Xu, M.; Zheng, H. S.; Huang, D.; Weng, Z. Q.; Tang, D. P. D-band-center-engineered platinum-based nanozyme for personalized pharmacovigilance. *Angew. Chem., Int. Ed.* **2025**, *64*, e202414625.

[48] Huang, L.; Chen, J. X.; Gan, L. F.; Wang, J.; Dong, S. J. Single-atom nanozymes. *Sci. Adv.* **2019**, *5*, eaav5490.

[49] Xu, Y.; Ma, Y. J.; Chen, X. H.; Wu, K. Q.; Wang, K. Y.; Shen, Y. F.; Liu, S. Q.; Gao, X. J. J.; Zhang, Y. J. Regulating reactive oxygen intermediates of Fe−N−C SAzyme via second-shell coordination for selective aerobic oxidation reactions. *Angew. Chem., Int. Ed.* **2024**, *63*, e202408935.

[50] Wu, L. F.; Lin, J. Y.; Wang, H. S.; Pan, K. Y.; Shi, X. M.; Niu, X. D. Portable colorimetric sensor array based on a porous single-atom Fe nanozyme with different surface sites for identifying artificially ripened fruits. *Adv. Funct. Mater.* **2025**, *35*, 2413154.

[51] Wu, F. L.; Wang, H. S.; Lv, J. H.; Shi, X. M.; Wu, L. F.; Niu, X. D. Colorimetric sensor array based on Au_2Pt nanozymes for antioxidant nutrition quality evaluation in food. *Biosens. Bioelectron.* **2023**, *236*, 115417.

[52] Zhao, Q. L.; Luan, T.; Sun, J.; Huang, J. S.; Du, Y.; Yang, X. R. Cu-based nanozyme-enabled triple channel colorimetric sensor arrays for efficient discrimination of flavonoids. *Anal. Chem.* **2025**, *97*, 19038-19046.

© The Author(s) 2026. *Nano Research* published by Tsinghua University Press. The articles published in this open access journal are distributed under the terms of the Creative Commons Attribution 4.0 International License (http://creativecommons.org/licenses/by/4.0/), which permits use, distribution and reproduction in any medium, provided the original work is properly cited.

Just Accepted

Electronic Supplementary Material

Tuning Mn–O covalency by ion intercalation to boost the oxidase-like activity of birnessite

Yao-Yao Chen,[1,2] Bo-Han Yao,[1,2] Qi-Lin Zhao,[1,2] Li-Min Ma,[1,2] Rui Han,[1,2] Dong-Ming Xu,[1,2] Chun-Xia Ma,[1,2] Bing Zhang,[1,2] Zhi-Ying Jin,[1,2] Dong-Xu Jiao,[3] Huan-Huan Xing,[4] De-Wen Wang,✉,[1] and Xiu-Rong Yang✉,[1,2]

[1] *State Key Laboratory of Electroanalytical Chemistry, Changchun Institute of Applied Chemistry, Chinese Academy of Sciences, Changchun 130022, China*
[2] *School of Applied Chemistry and Engineering, University of Science and Technology of China, Hefei 230026, China*
[3] *College of Chemistry, Chemical Engineering and Resource Utilization, Northeast Forestry University, Harbin 150040, China*
[4] *School of Materials Science and Engineering, Suzhou University of Science and Technology, Suzhou 215009, China*

✉Address correspondence to Xiu-Rong Yang, xryang@ciac.ac.cn; De-Wen Wang, dwwang@ciac.ac.cn

Supporting information to https://doi.org/10.26599/NR.2026.94909224

Just Accepted

1. Materials and Apparatuses

1.1 Materials

All of the chemicals used in this study were purchased from commercial vendors and used without further purification. Potassium permanganate ($KMnO_4$), hydrochloric acid (HCl), magnesium chloride hexahydrate ($MgCl_2·6H_2O$), calcium chloride anhydrous ($CaCl_2$), strontium dichloride hexahydrate ($SrCl_2·6H_2O$), barium chloride dihydrate ($BaCl_2·2H_2O$), n-Butanol, acetic acid (HAc) and sodium acetate (NaAc) were purchased from Xilong Science Co, Ltd (China). 3,3′,5,5′-tetramethylbenzidine (TMB), L-Tryptophan (Trp), p-Benzoquinone (p-BQ), tannic acid (TA), (-)-Epigallocatechin (EGC), gallic acid (GA), L-Cysteine (CYS), sodium chloride (NaCl), potassium chloride (KCl), natrual β-Carotene, glycine and lysine were obtained from Aladdin Industrial Corporation (China). L-Ascorbic acid (AA), glucose and sodium citrate tribasic dihydrate were supplied by Aladdin Industrial Corporation (China). Commercial water soluble c100, oriental leaf tea drink and milk are purchased in supermarket. The ultrapure water (18.25 MΩ·cm) used in the experiments was produced by a Milli-Q water system.

1.2 Apparatuses

Scanning Electron Microscopy (SEM). All the SEM images of the samples were gained by a XL30 ESEM FEG microscope at an accelerating voltage of 20 kV.

Transmission Electron Microscopy (TEM). TEM images were captured by a JEM-2010 microscope at accelerating voltage of 200 kV. Energy-dispersive X-ray spectroscopic (EDS) mappings were obtained with a probe corrected JEOL ARM200F microscopy operated at 200 kV.

X-ray Diffraction (XRD). XRD data were acquired on a RigakuD/MAX 2550 diffractometer with Cu K_α radiation (λ=1.5418 Å).

X-ray Photoelectron Spectroscopy (XPS). XPS measurements were conducted using an ESCALAB MK II X-ray photoelectron spectrometer with Mg as the excitation source.

Fourier-transform Infrared Spectroscopy (FT-IR). FT-IR spectra were conducted on a Bruker Optics VERTEX 70 spectrometer (Germany).

Zeta Potential. All the measurements of zeta potential were carried out on a Malvern Zetasizer from Malvern Instrument Ltd (UK).

Inductively Coupled Plasma Optical Emission Spectrometry (ICP-OES). The content of Mg, Ca, Sr and Ba in the catalyst were determined using ICP-OES, Thermo ICAP 6300.

Gas Sorption. Gas adsorption isotherms were collected by an Autosorb iQ Station 2 surface characterization analyzer from Quantachrome (USA). The nitrogen adsorption and desorption isotherms were measured at 77.35 K, and the Brunauer-Emmet-Teller (BET) surface area was analyzed and calculated by Quantachrome® ASiQwin™.

Electron Paramagnetic Resonance (EPR). The oxygen vacancy relative intensity and the corresponding control reactive oxygen species (ROS)-trapping experiments were measured by EPR spectra that performed on JES-FA300.

X-ray Absorption Spectroscopy (XAS). The X-ray absorption fine structure (XAFS) spectra of Mn *K*-edge were collected at station 1W1B of the Beijing Synchrotron Radiation Facility (BSRF). The storage ring of BSRF operates at 2.5 GeV with an average current of 250 mA. A Si (111) double-crystal monochromator was used, and data were collected in transmission/fluorescence mode using an ionization chamber. All spectra were acquired under ambient conditions. The XAFS spectra were analyzed using the Athena and Artemis. The calculation of wavelet transformation of extended X-ray absorption fine structure (EXAFS) spectra was performed with Hama Fortran program.1.0.

Ultraviolet–visible (UV-vis) absorption Spectroscopy. The UV-vis spectra were collected on Cary 50 UV-vis-NIR spectrophotometer (Varian) and Spark™ Multimode Microplate reader (Tecan, Männedorf, Switzerland) in absorbance and absorbance scan mode.

1. Experimental sections

1.1 Preparations of catalysts

Synthesis of Birnessite. Hydrochloric acid (4 M, 50.0 mL) was added drop wise via a syringe pump at 1 mL/min to a heated and stirred (80 ˚C, 360 rpm) solution of potassium permanganate ($KMnO_4$, 0.2 M, 250 mL) in a 400 mL beaker. Heating continued at 80 ˚C for an

additional 0.5 h after addition was completed. The resulting 300 mL solution was then covered to prevent excessive evaporation overnight and aged for 15 h at 50 ˚C. Finally, the resulting suspension was washed several times with distilled water.

Synthesis of MgBir, CaBir, SrBir and BaBir. 80 mg Birnessite was dispersed in deionized water. Then, 87 μL of 1 M magnesium chloride hexahydrate ($MgCl_2·6H_2O$) was added drop wise into the mixture under intensely stirring and keep continuous stir for 24 h under room temperature. The solid was collected and washed several times with distilled water. CaBir, SrBir and BaBir were synthesized in the same method, expect $CaCl_2$, $SrCl_2·6H_2O$ and $BaCl_2·2H_2O$ were used as precursor, respectively.

Oxidase-like activity

The oxidase-mimicking activity was evaluated by using TMB as substrate at 25 °C under acidic conditions (pH 4.0, 0.2 M HAc-NaAc buffer). In detail, 10 μL of various catalysts aqueous solution (1 mg mL^{-1}) and 10 μL of TMB (10 mg mL^{-1} in DMSO) were sequentially added into 980 uL HAc-NaAc buffer (0.2 M, pH 4.0). The absorbance of TMBox was recorded at 652 nm through Cary-50 UV-vis spectrophotometer.

Enzymatic kinetic analysis

To characterize the kinetic of catalysts, the TMB was added into the reaction at the final concentrations of 0.05 mM, 0.1 mM, 0.2 mM, 0.4 mM, 0.8 mM, and 1.6 mM TMB. The absorbance values at 652 nm were continuously detected by a microplate reader to calculate the initial reaction speed at different TMB concentrations. The kinetic constants (K_m and V_{max}) were obtained according to Michaelis-Menten equation:

$$V = V_{max}[S]/(K_m + [S])$$

where V is the initial velocity, [S] is the concentration of the substrate, K_m is the Michaelis-Menten constant, and V_{max} is the maximal reaction velocity.

Specific activity calculation

Calculate the nanozyme activity (units) using the following equation:

$$b=V/(\varepsilon\times l)\times(\Delta A/\Delta t)$$

where b is the catalytic activity of nanozyme expressed in units. Our unit was defined as the amount of nanozyme that catalytically produces 1 μM of product per min at room temperature. V is the total volume of reaction solution (μL); ε is the molar absorption coefficient of the colorimetric substrate, which is maximized at 39,000 M^{-1} cm^{-1} at 652 nm for TMB; l is the path length of light traveling in the cuvette (cm); A is the absorbance after subtraction of the blank value; and $\Delta A/\Delta t$ is the initial rate of change in absorbance at 652 nm·min^{-1}.

Calculate the specific activity of the nanozyme (U mg^{-1}) by

$$a=b/[m]$$

where a is the specific activity expressed in units per milligram (U·mg^{-1}) nanozymes, and [m] is the nanozyme weight (mg) of each assay.

Catalytic mechanism

The influences of various scavengers on the oxidase-like activity were investigated by comparing the activity in the absence or presence of ROS scavengers. In the catalytic oxidation of TMB, the Birnessite was added into the HAc-NaAc buffer (pH 4.0) system containing n-Butanol, Tryptophan (Trp) and 1,4-Benzoquinone (p-BQ) with distinct contents. Then, the absorbance at 652 nm was measured respectively.

Density functional theory calculation

All spin-polarized density functional theory (DFT) calculations were carried out with the plane-wave basis set as implemented in the Vienna Ab Initio Simulation Package (VASP), and the electrons and ions interactions were described by the projector augmented wave (PAW) potential. The exchange–correlation interactions were determined by the Perdew-Burke-Ernzerhof (PBE) functional within the generalized gradient approximation (GGA). The plane wave energy cutoff of 500 eV, and the convergence criterion for the residual force and energy was set to 0.05 eV $Å^{-1}$ and 10^{-5} eV, respectively. The empirical correction in Grimme's method (DFT+D3) was used to describe the van der Waals (vdW) interactions. The Brillouin region was sampled by the Monkhorst-Pack method with a 2 × 2 × 1 k-point mesh. The change in the Gibbs free energy change (ΔG) for each possible step during the electrochemical synthesis of urea was obtained using the computational hydrogen electrode (CHE) model. The changes in Gibbs free energy (ΔG) for all electrochemical steps was defined as:

$$\Delta G = \Delta E + \Delta E_{ZPE} - T\Delta S$$

where the reaction energy (ΔE) can be directly obtained by analyzing the DFT total energies. The zero-point energy difference (ΔE_{ZPE}) between the products and the reactants can be computed from the vibrational frequencies. ΔS is the change in entropy between the products and the reactants at room temperature (T = 298.15 K).

Construction of the colorimetric sensor array for antioxidant identification

HAc-NaAc buffer solution (pH =4.0), Birnessite/SrBir/MgBir, different kinds (TA, AA, EGC, GC and CYS) and different concentrations (6, 16, 28, 40 and 50 μmol L^{-1}) of antioxidants were added to the 96 well plate and the absorbance at 652 nm was measured with the microplate reader. This process was repeated for five antioxidants to generate six replicates. Therefore, the antioxidants were tested at different catalysts to produce 3 × 5 × 6 data matrix.

Discrimination of binary and ternary antioxidant mixtures

Typically, different ratio of binary or ternary antioxidant mixtures with a total concentration of 28 μmol L^{-1} were introduced to the system. Other experimental and data processing procedures were kept the same as the construction of sensor arrays.

Anti-interference capability of the sensor array

To evaluate the anti-interference capability of the sensor array, 7 potential interferents (sodium chloride, potassium chloride, natural β-carotene, glycine, lysine, glucose, and trisodium citrate dihydrate) were introduced to the sensor array with a concentration of 28 μmol L^{-1}.

Identification of content in real samples

Commercial water soluble c100 and oriental leaf tea drink were pretreated by centrifugation. The liquid milk sample (25.0 g) was mixed with 5 mL $K_4[Fe(CN)_6]$ solution (0.30 mol L^{-1}) and 5 mL $Zn(Ac)_2$ solution (1.2 mol L^{-1}). And then adjust the volume to 100 mL with ultrapure water. After filtering, the filtrate was stored in a refrigerator at 4 °C.

NSR Accepted

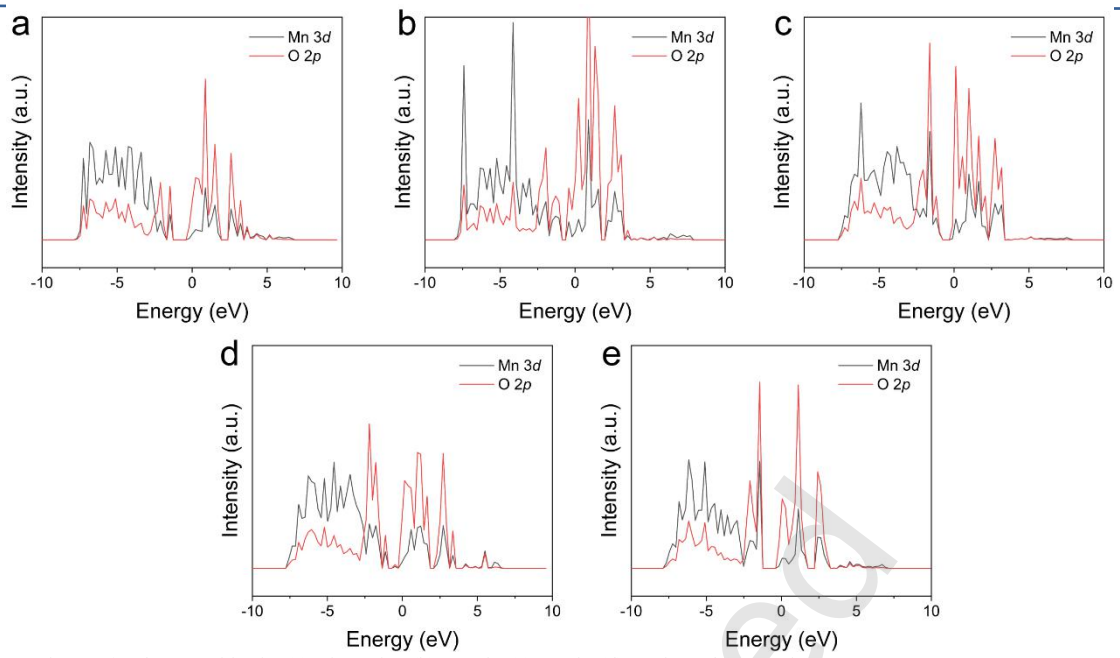


Figure S1. PDOS of Mn 3*d* and O 2*p* orbits for (a) Birnessite, (b) MgBir, (c) CaBir, (d) SrBir, and (e) BaBir.

Just Accepted

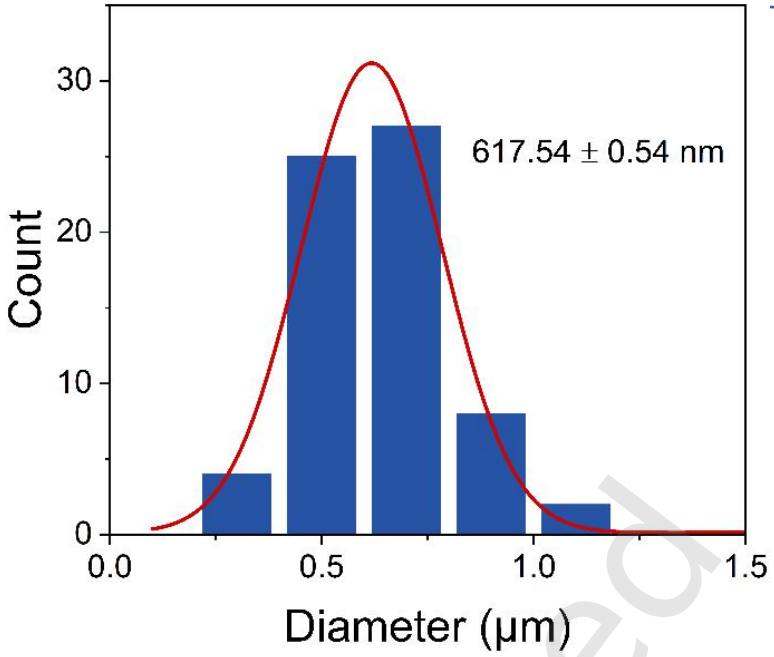


Figure S2. Histogram of size distribution of Birnessite.

Just Accepted

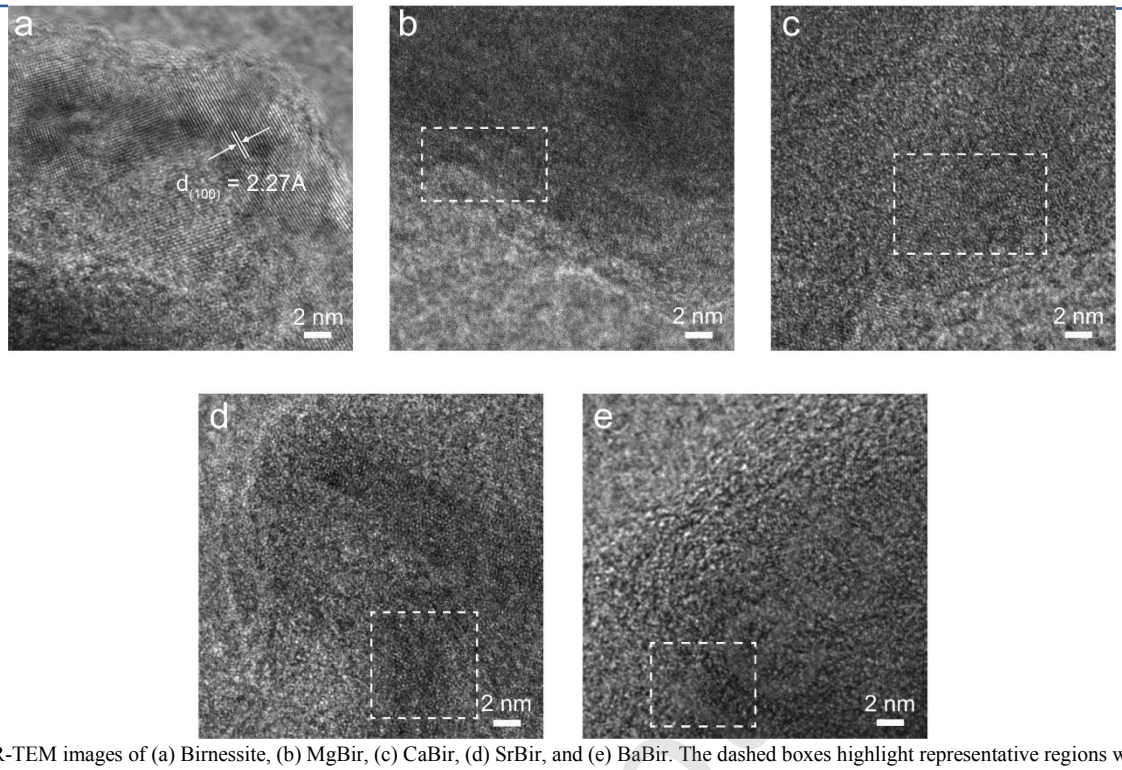


Figure S3. HR-TEM images of (a) Birnessite, (b) MgBir, (c) CaBir, (d) SrBir, and (e) BaBir. The dashed boxes highlight representative regions with blurred lattice fringes.

The blurred lattice fringes observed throughout the ion-intercalated samples indicate the presence of bulk static disorder in the lattice. DFT calculations attribute this static disorder to the generation of oxygen vacancies, which induce local relaxation of the surrounding Mn-O octahedra. This interpretation is consistent with the XRD data, which show negligible peak broadening but notable intensity attenuation upon ion intercalation.

Just Accepted

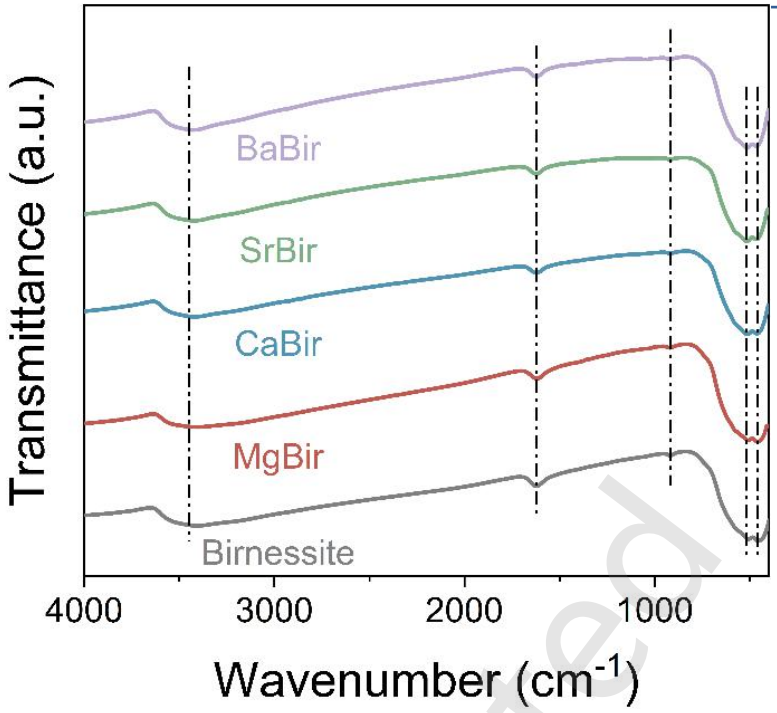


Figure S4. FT-IR spectra of Birnessite, MgBir, CaBir, SrBir, and BaBir.

Just Accepted

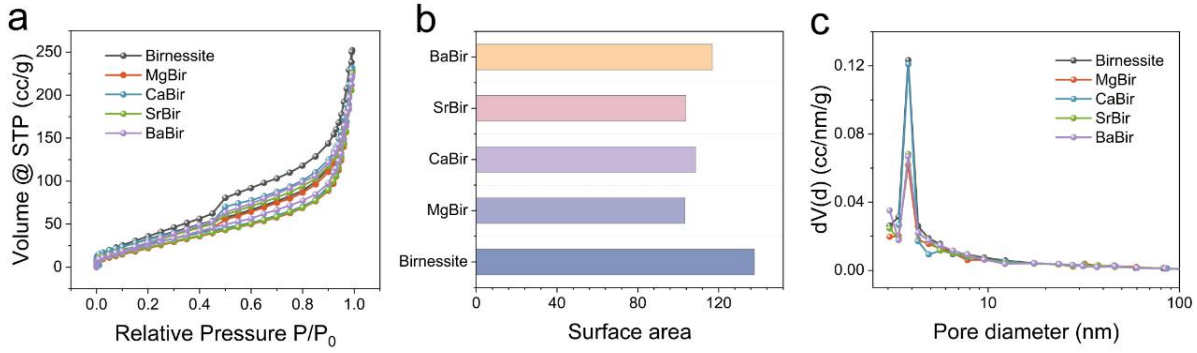


Figure S5. (a) N_2 adsorption/desorption isotherms, (b)surface areas, (c) and pore size distribution curves of Birnessite, MgBir, CaBir, SrBir, and BaBir.

Just Accepted

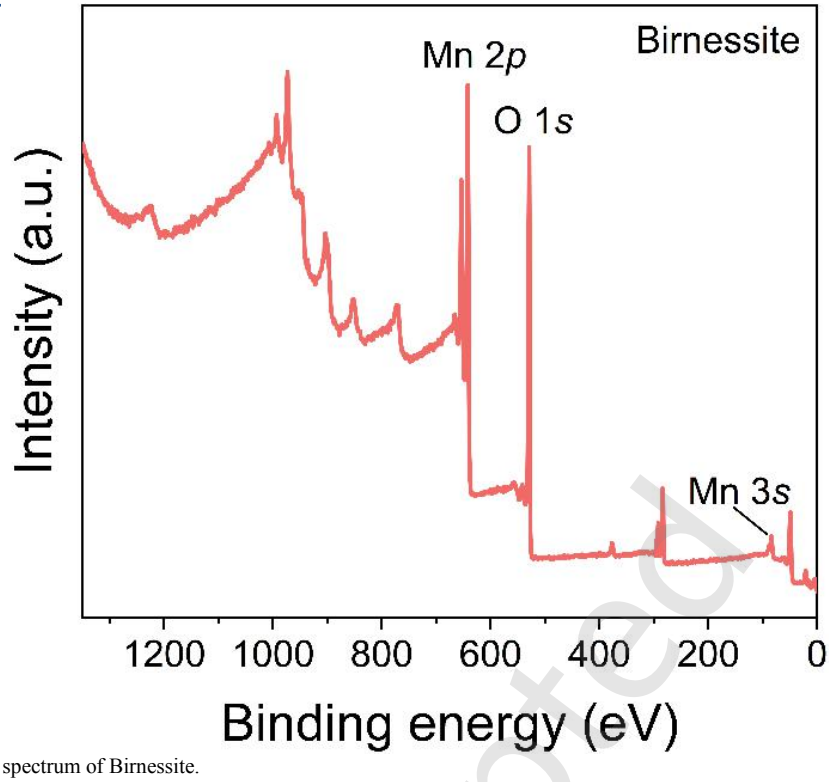


Figure S6. The XPS wide scan spectrum of Birnessite.

Just Accepted

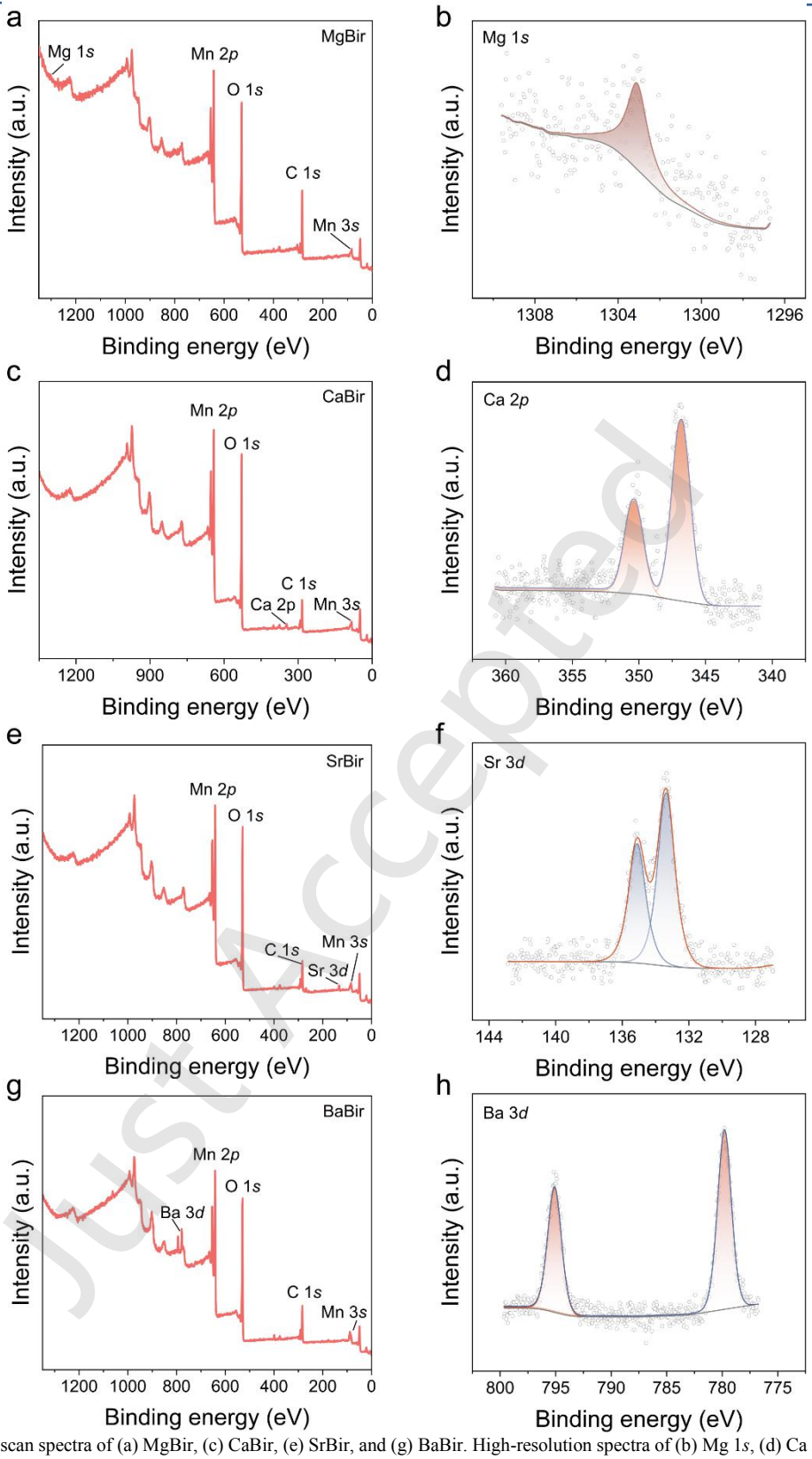


Figure S7. The XPS wide scan spectra of (a) MgBir, (c) CaBir, (e) SrBir, and (g) BaBir. High-resolution spectra of (b) Mg 1*s*, (d) Ca $2p_{3/2}$, (f)Sr $3d_{5/2}$, and (h)Ba $3d_{5/2}$.

Just Accepted

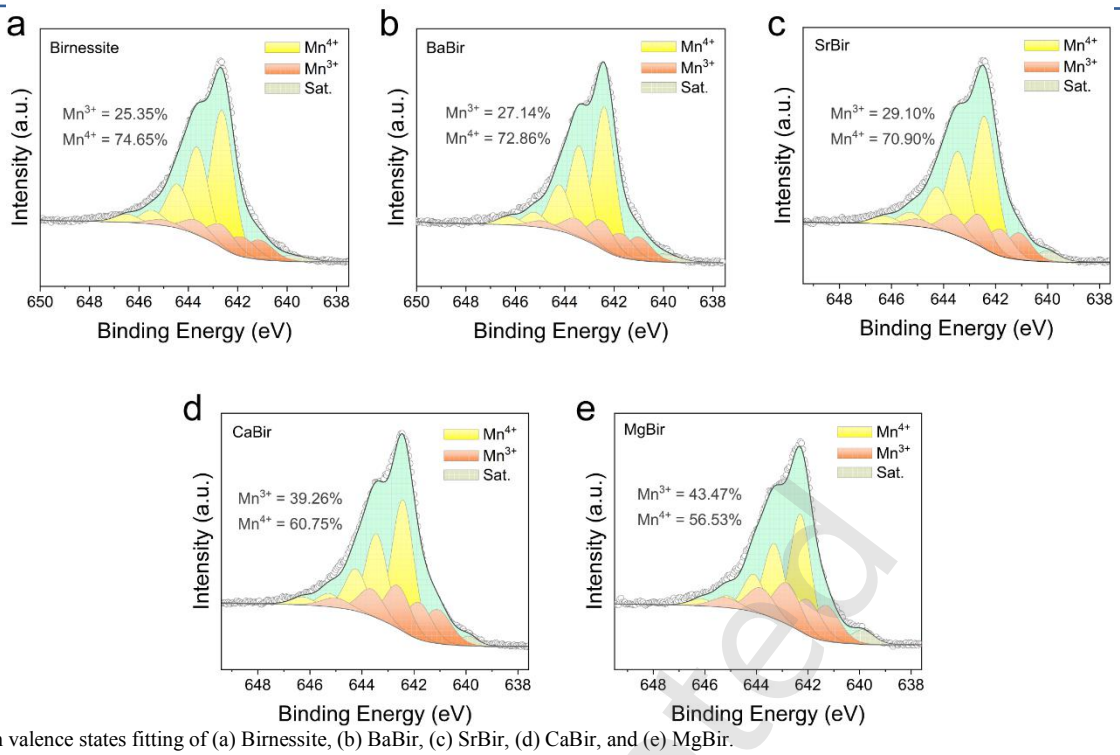


Figure S8. Mn valence states fitting of (a) Birnessite, (b) BaBir, (c) SrBir, (d) CaBir, and (e) MgBir.

The average Mn oxidation state was obtained from the fitted Mn $2p_{3/2}$ XPS spectra. Specifically, the Mn $2p_{3/2}$ spectrum was deconvoluted into Mn^{3+} and Mn^{4+} species. The relative fractions of each oxidation state were obtained from the integrated peak areas. The average Mn oxidation state was then calculated using the following equation:

$$Average\ Mn\ oxidation\ state = (3 \times A(Mn^{3+}) + 4 \times A(Mn^{4+}))/(A(Mn^{3+}) + A(Mn^{4+}))$$

$A(Mn^{3+})$ and $A(Mn^{4+})$ represent the integrated areas.

Just Accepted

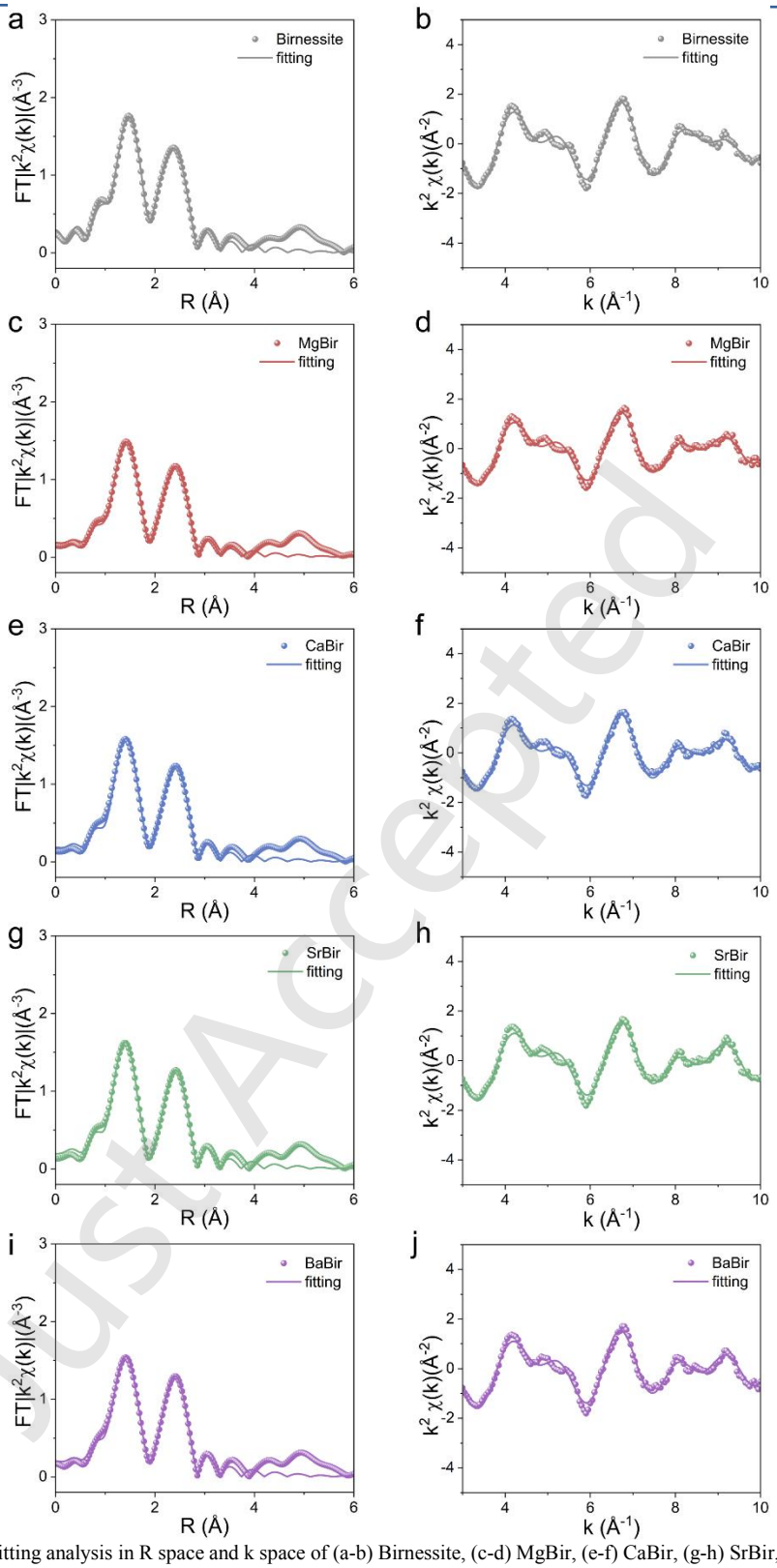


Figure S9. Mn *K*-edge EXAFS fitting analysis in R space and k space of (a-b) Birnessite, (c-d) MgBir, (e-f) CaBir, (g-h) SrBir, and (h-i) BaBir.

Just Accepted

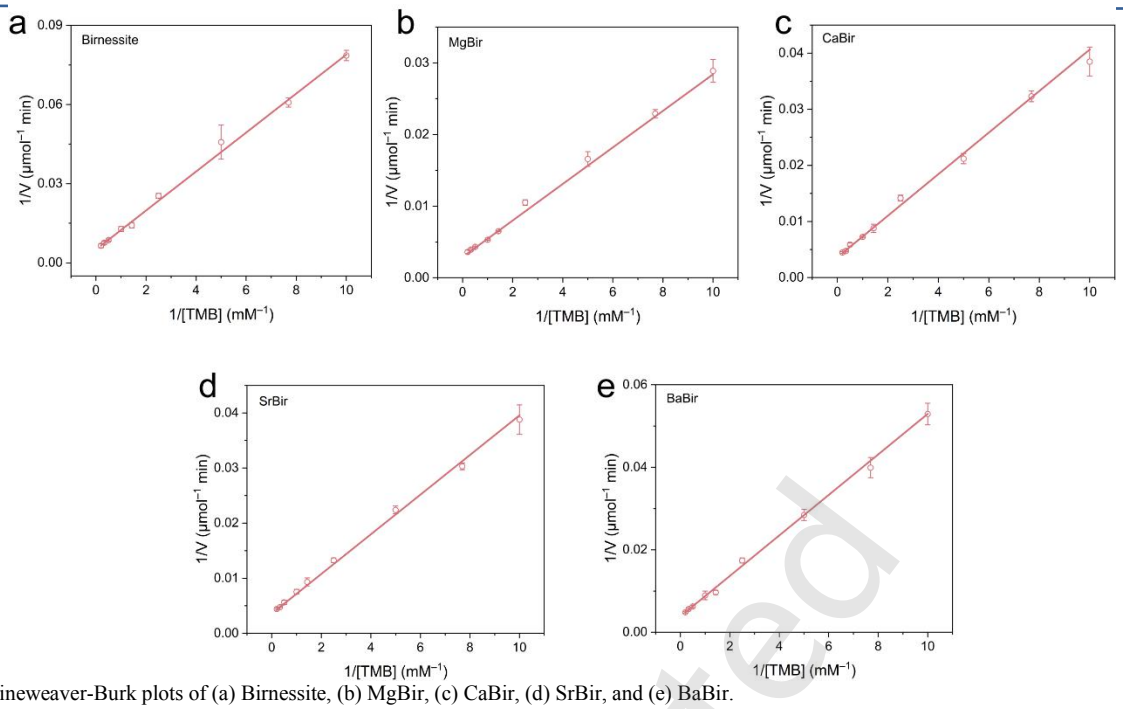


Figure S10. Lineweaver-Burk plots of (a) Birnessite, (b) MgBir, (c) CaBir, (d) SrBir, and (e) BaBir.

Just Accepted

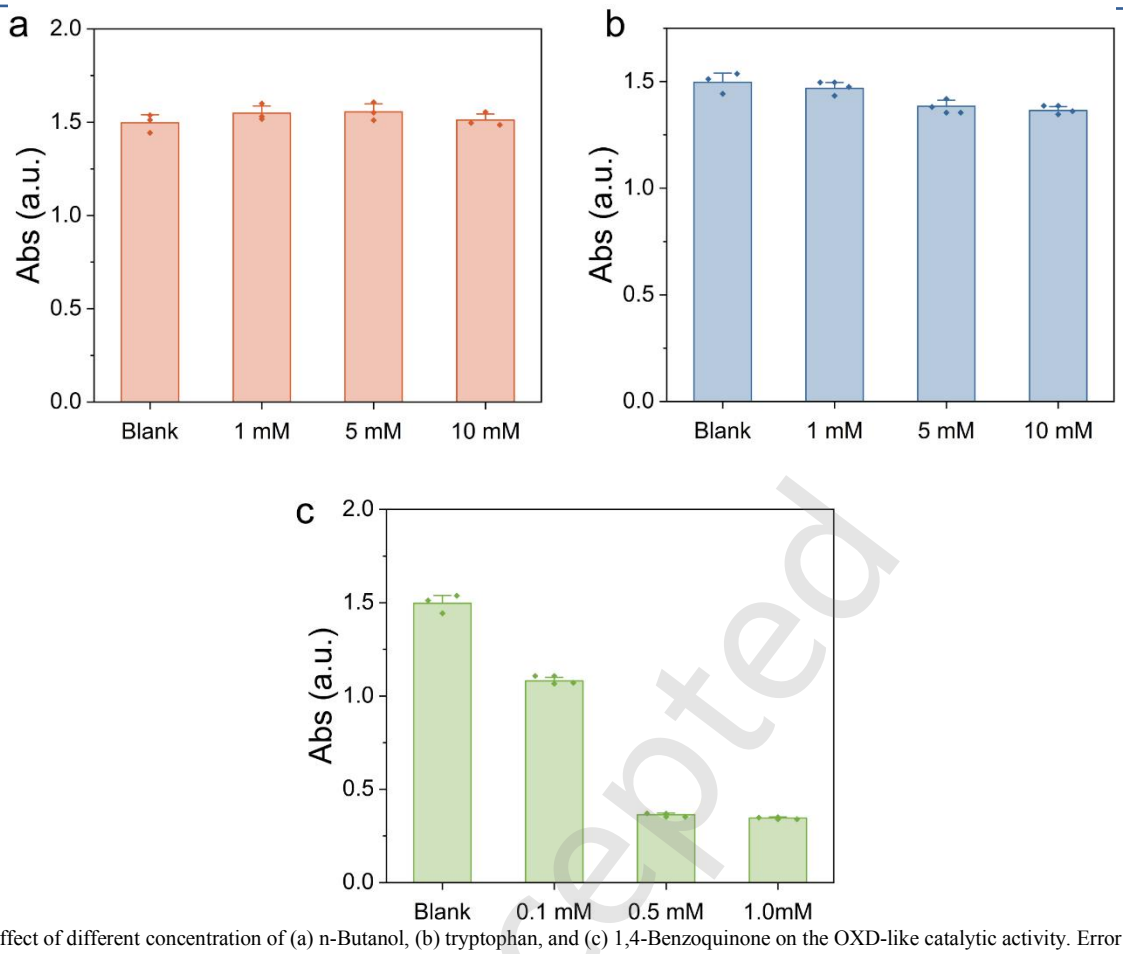


Figure S11. Effect of different concentration of (a) n-Butanol, (b) tryptophan, and (c) 1,4-Benzoquinone on the OXD-like catalytic activity. Error bars indicate ± SD.

Just Accepted

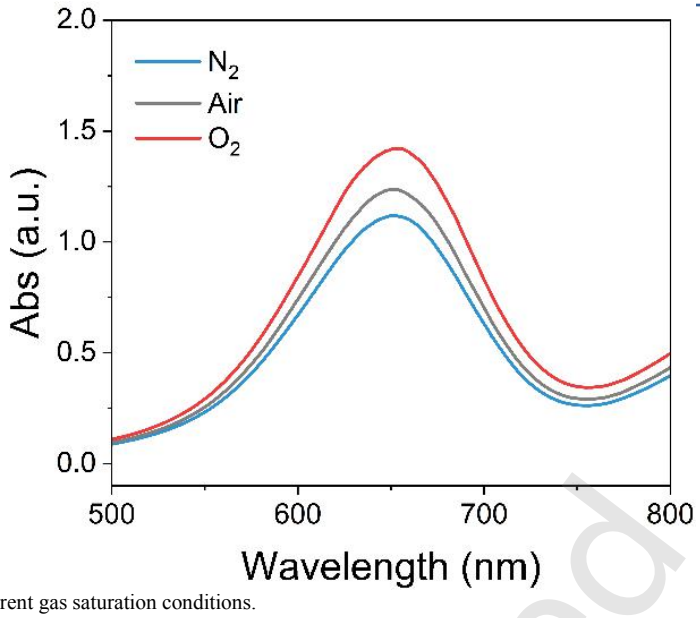


Figure S12. UV-vis spectra under different gas saturation conditions.

Just Accepted

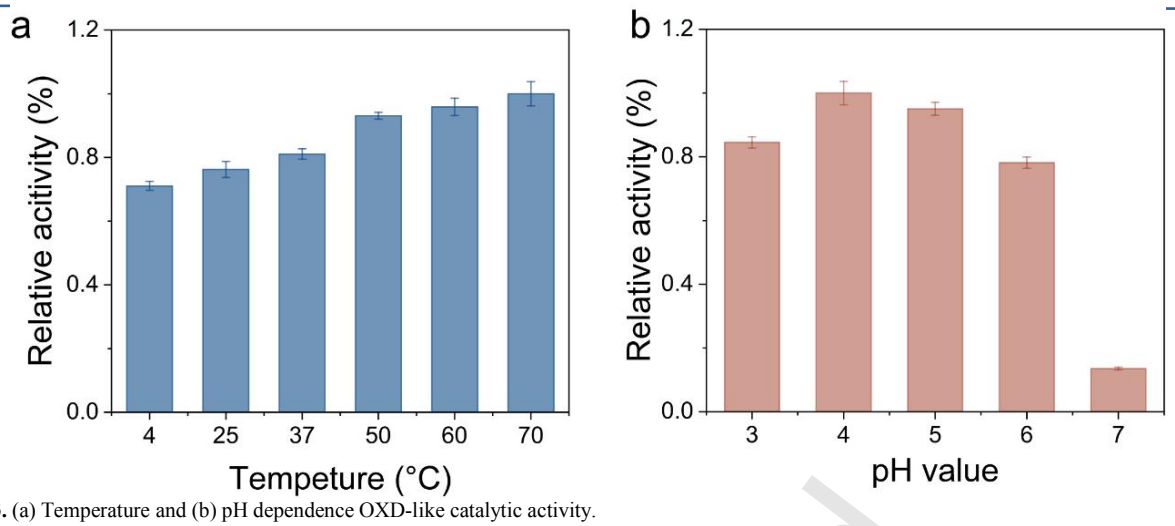


Figure S13. (a) Temperature and (b) pH dependence OXD-like catalytic activity.

Just Accepted

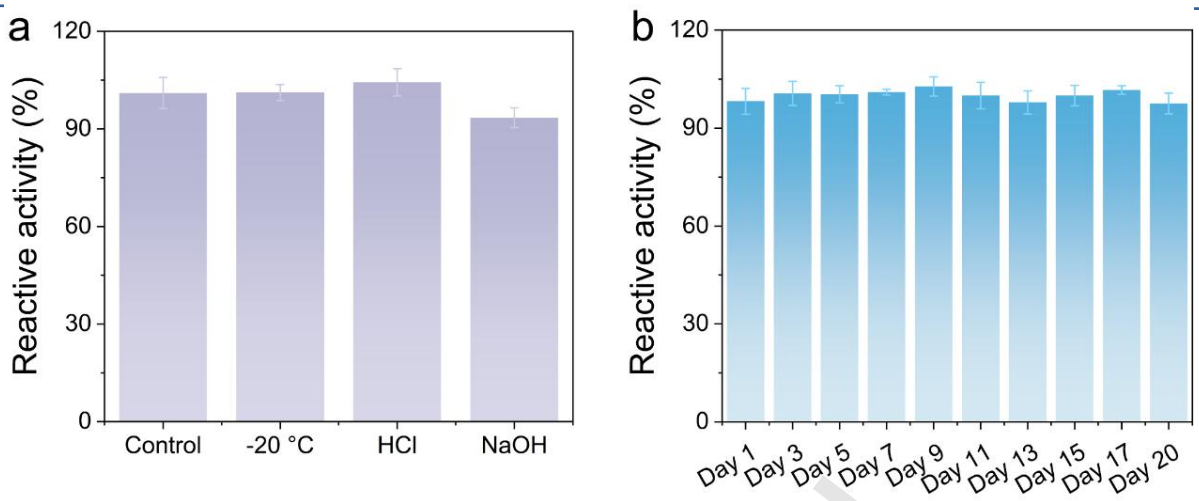


Figure S14. (a) Chemical stability. The experimental conditions of "–20 °C" is mixing nanozyme with ultrapure water (18.25 MΩ·cm) and cryogenic freezing it to –20°C for 24 h. (b) Storage duration stability of the catalyst.

Just Accepted

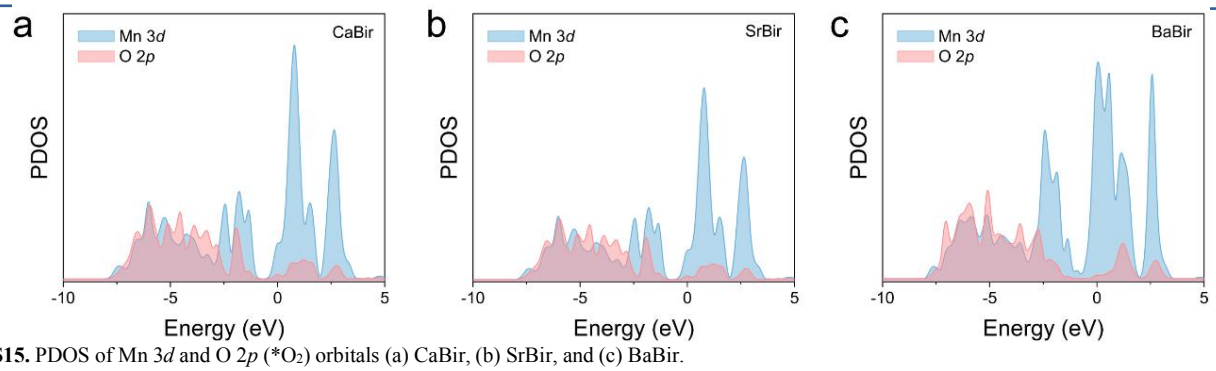


Figure S15. PDOS of Mn 3*d* and O 2*p* (*O_2) orbitals (a) CaBir, (b) SrBir, and (c) BaBir.

Just Accepted

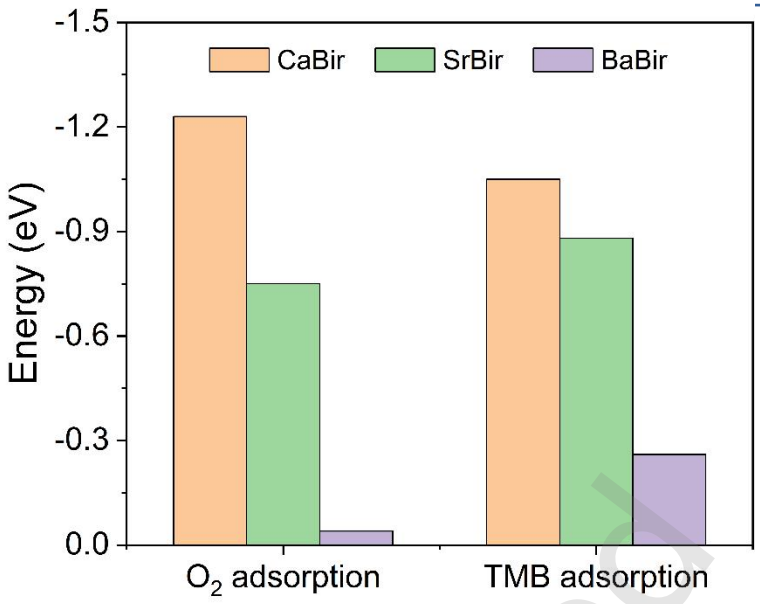


Figure S16. The calculated O_2 adsorption energies and TMB absorption energies.

Just Accepted

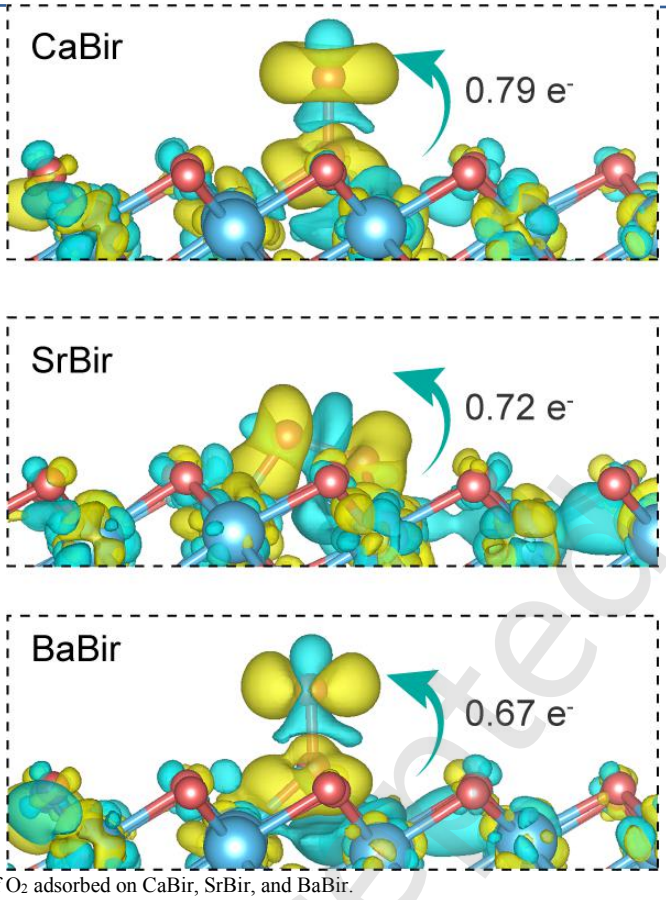


Figure S17. Charge density difference of O_2 adsorbed on CaBir, SrBir, and BaBir.

Just Accepted

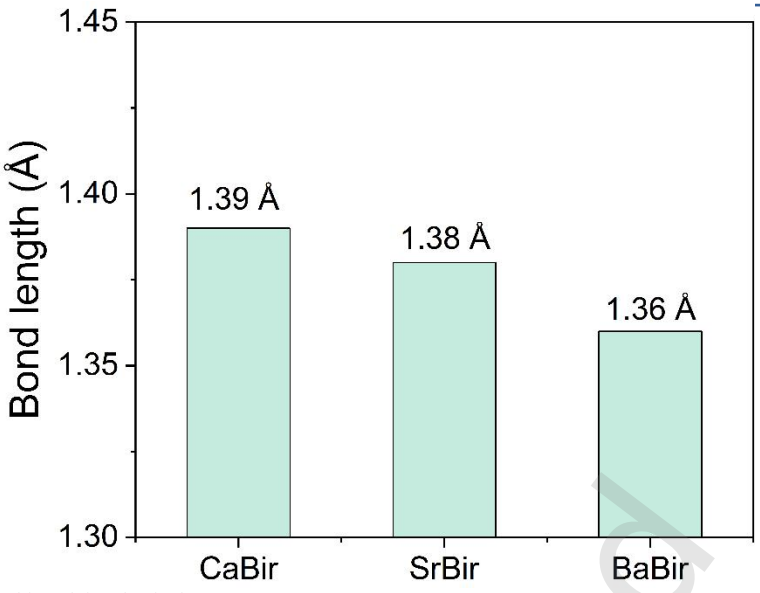


Figure S18. The calculated O–O bond length in adsorbed O_2.

Just Accepted

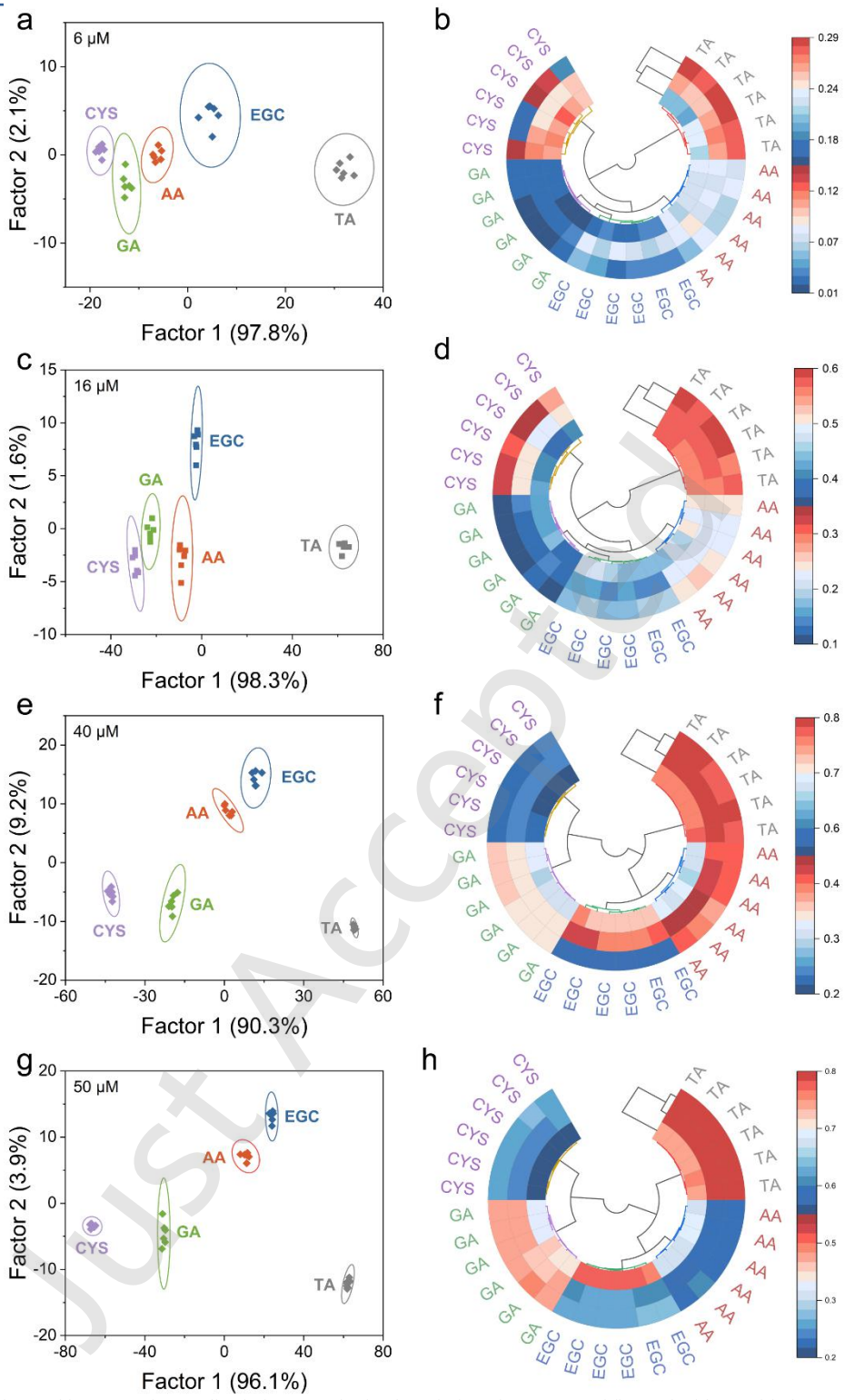


Figure S19. LDA score plots and heatmap of HCA discriminant results for the colorimetric response of five antioxidants with the sensor array at different concentrations: (a-b) 6 μmol L^{-1}, (c-d) 16 μmol L^{-1}, (e-f) 40 μmol L^{-1}, and (g-h) 50 μmol L^{-1}.

Just Accepted

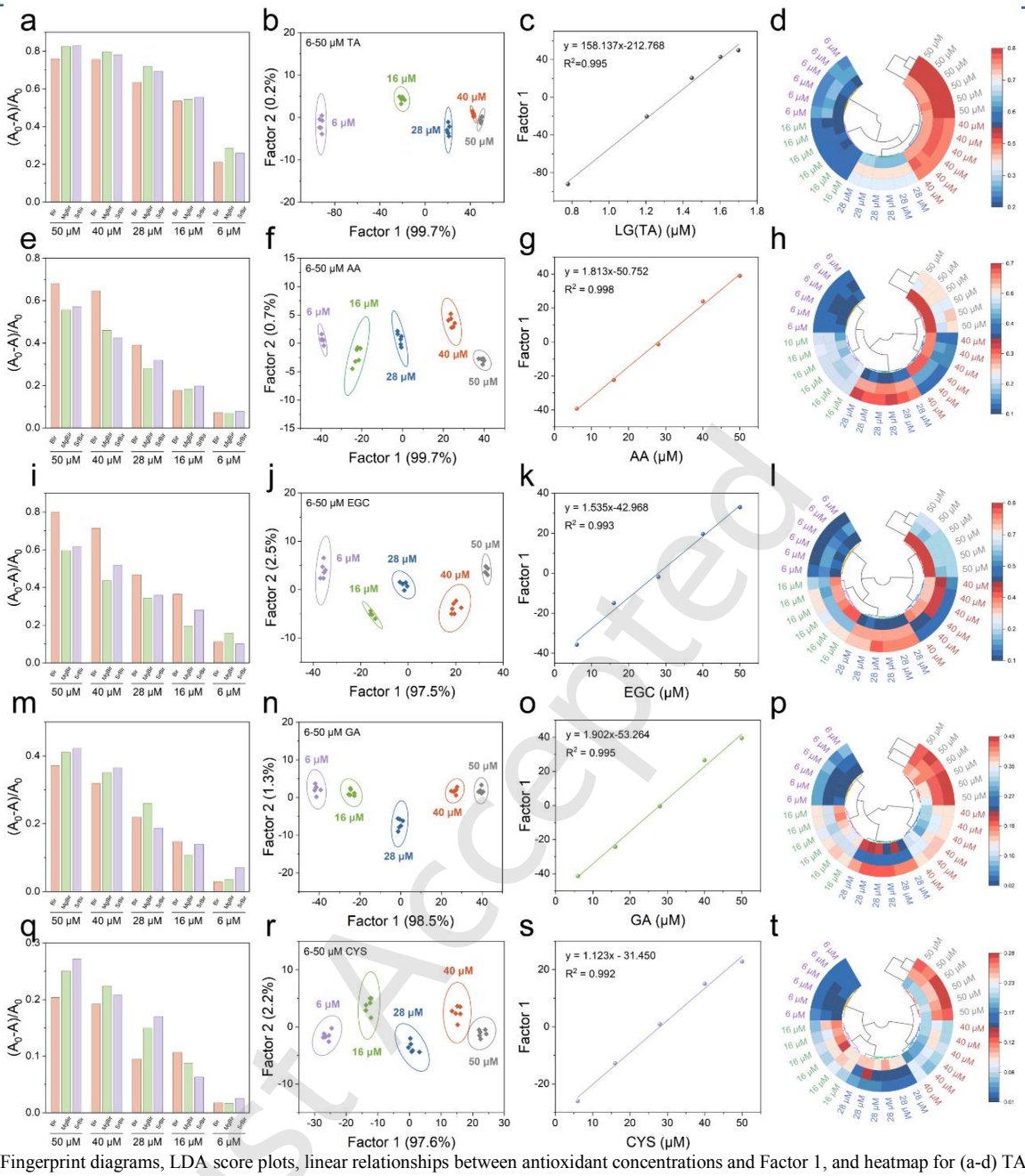


Figure S20. Fingerprint diagrams, LDA score plots, linear relationships between antioxidant concentrations and Factor 1, and heatmap for (a-d) TA, (e-h) AA, (i-l) EGC, (m-p) GA, and (q-t) CYS.

Just Accepted

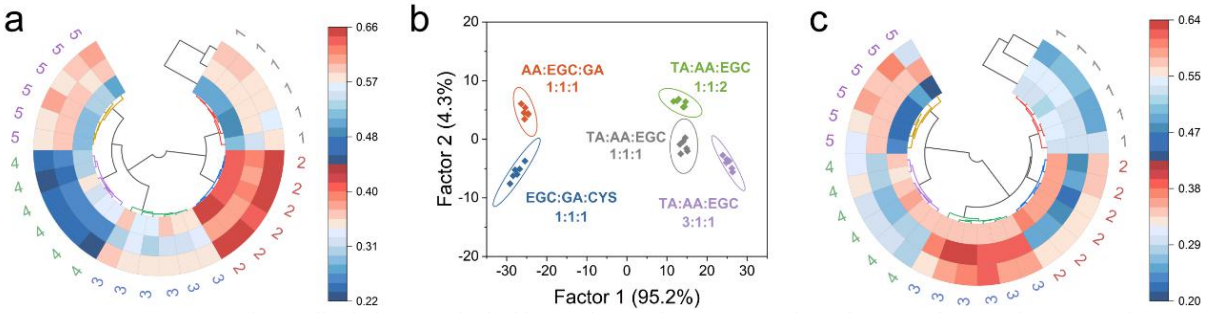


Figure S21. (a) Heatmap of HCA discriminant results for binary mixtures (b) LDA score plot and (c) HCA heatmap for ternary mixtures**.**

Just Accepted

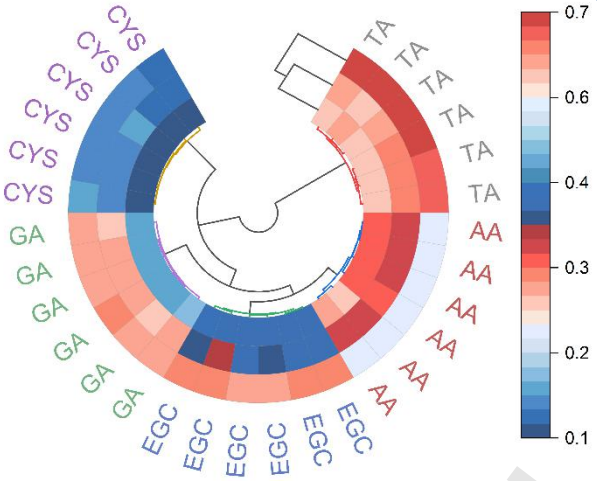


Figure S22. Heatmap of HCA discriminant results for anti-interference assay**.**

Just Accepted

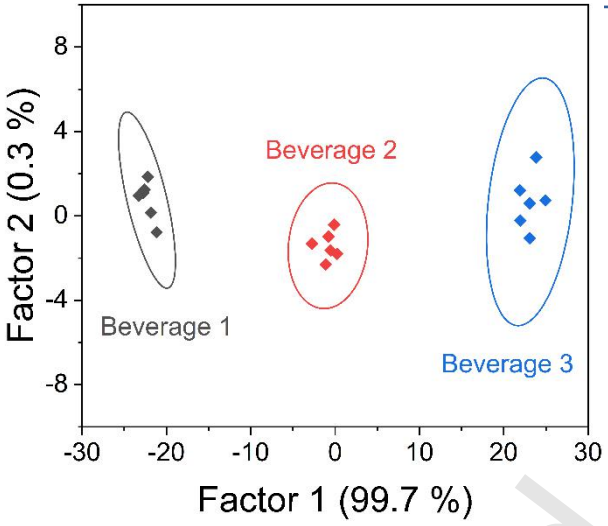


Figure S23. LDA score plot for real samples assay**.**
Beverage 1: water soluble c100, the principal antioxidant components are ascorbic acid. Beverage 2: oriental leaf tea drink, the principal antioxidant components are tea polyphenol. Beverage 3: milk, the principal antioxidant components are cysteine.

Just Accepted

Table S1. Element content quantified by ICP-OES.

Element / Samples	Mg (ppm)	Ca (ppm)	Sr (ppm)	Ba (ppm)	Mn (ppm)
MgBir	**7551**	**-**	**-**	**-**	**531630**
CaBir	**-**	**18840**	**-**	**-**	**533330**
SrBir	**-**	**-**	**36560**	**-**	**516109**
BaBir	**-**	**-**	**-**	**95670**	**516354**
Birnessite	**-**	**-**	**-**	**-**	**547874**

Just Accepted

Table S2. EXAFS fitting parameters at the Mn *K*-edge for various samples (S_0^2=0.95).

	Path	CN[a]	R (Å) [b]	σ^2 (Å^{-2}) [c]	ΔE_0 (eV) [d]	R factor[e]
Mn-foil	**Mn-Mn**	**12***	**2.95±0.01**	**0.0035**	**1.3±2.0**	**0.006**
Mn-Birnessite	**Mn–O**	**5.74±0.1**	**1.96±0.03**	**0.0076**	**1.20±0.23**	**0.004**
	Mn–Mn	**3.68±0.1**	**2.95±0.01**	**0.0052**		
Mn-MgBir	**Mn–O**	**4.69±0.1**	**1.82±0.06**	**0.0072**	**0.95±0.21**	**0.003**
	Mn–Mn	**3.45±0.1**	**3.06±0.05**	**0.0067**		
Mn-CaBir	**Mn–O**	**4.95±0.1**	**1.83±0.06**	**0.0072**	**0.22±0.19**	**0.003**
	Mn–Mn	**3.53±0.1**	**3.05±0.04**	**0.0064**		
Mn-SrBir	**Mn–O**	**5.12±0.1**	**1.84±0.05**	**0.0049**	**1.02±0.31**	**0.009**
	Mn–Mn	**3.64±0.1**	**3.04±0.03**	**0.0062**		
Mn-BaBir	**Mn–O**	**5.54±0.1**	**1.86±0.03**	**0.0036**	**3.2±1.7**	**0.013**
	Mn–Mn	**3.65±0.1**	**3.03±0.01**	**0.0054**		

[a]*CN*: Mn ordination numbers; [b]*R*: bond distance; [c]σ^2: Debye-Waller factors; [d] ΔE_0: the inner potential correction. R factor: goodness of fit. Error bounds that characterize the structural parameters obtained by EXAFS spectroscopy were estimated as CN±20%; R ± 1%; σ^2 ± 20%. The obtained XAFS data was processed in Athena (version 0.9.25) for background, pre-edge line and post-edge line calibrations. Then Fourier transformed fitting was carried out in Artemis (version 0.950). The k^2 weighting, k-range of 3–10 Å^{-1} and R range of 1– ~4 Å were used for the fitting. The four parameters, coordination number, bond length, Debye-Waller factor and E_0 shift (CN, R, σ^2, ΔE_0) were fitted without anyone was fixed, constrained, or correlated.

Just Accepted

Table S3. Enzyme kinetic parameters of various samples as OXD mimics.

	K_m (mM)	V_{max} (μmol min^{-1})
MgBir	**0.88**	**344.84**
CaBir	**1.00**	**277.25**
SrBir	**1.01**	**268.23**
BaBir	**1.17**	**251.18**
Birnessite	**1.47**	**197.86**

Just Accepted

Table S4. Comparison of the kinetic parameters of various OXD mimics.

Number	Materials	Substrate	K_m (mM)	V_{max} (μmol min^{-1})	Ref.
1	Mn/PSAE	TMB	0.11	4.20	1
2	Mn_{SA}-N_3-C	TMB	1.17	29.24	2
3	pFeSAN	TMB	0.17	100.20	3
4	Fe/NC-800	TMB	0.17	5.34	4
5	FePc@2D-Cu–N–C	TMB	0.60	53.48	5
6	Fe-N/C	TMB	0.94	35.88	6
7	FeNSC	TMB	0.24	22.80	7
8	Co-N-C SAzymes	TMB	0.15	0.64	8
9	Fe-N_4 pero-nanozysome	TMB	0.55	2.72	9
10	CoN_5 SA-CNF	TMB	0.68	10.62	10
11	Co_3O_4 nanoflowers	TMB	0.28	5.91	11
12	MdP	TMB	0.20	2.06	12
13	$CdCo_2O_4$	TMB	0.32	1.31	13
14	MnO_2-Silk films	TMB	1.62	160.00	14
15	OV-Mn_3O_4-NFS	TMB	1.66	2.38	15
16	Mn_3O_4-NFS	TMB	13.20	0.81	15
17	Nano-CeO_2	TMB	0.42	6.00	16
18	C-CoCu-HNC	TMB	0.07	1.54	17
19	Pt NCs	TMB	0.63	0.16	18
20	Ir nanoparticles	TMB	0.28	0.01	19
21	Se nanoparticles	TMB	8.30	0.18	20
22	La-RhRu	TMB	0.67	0.92	21
23	Pd12-cage	TMB	0.24	4.70	22
24	Ru NPs	TMB	54.93	0.60	23
25	Ce-MOF	TMB	0.09	6.60	24
26	Au@HCNs	TMB	0.18	2.94	25
27	MgBir	TMB	0.88	344.84	This work
28	CaBir	TMB	1.00	277.25	
29	SrBir	TMB	1.01	268.23	
30	BaBir	TMB	1.17	251.18	
31	Birnessite	TMB	1.47	197.86	

Just Accepted

Table S5. Calculated reaction energy of OXD-like reactions.

	Birnessite G (eV)	**BaBir G (eV)**	**SrBir G (eV)**	**CaBir G (eV)**	**MgBir G (eV)**
***OOH**	**-3.436**	**-1.967**	**-1.222**	**-2.281**	**-3.525**
***O**	**-5.104**	**-5.103**	**-4.418**	**-4.685**	**-5.067**
***OH**	**-6.867**	**-5.517**	**-5.370**	**-5.183**	**-5.088**

Just Accepted

References.

(1) Zhu, Y.; Wang, W.; Cheng, J.; Qu, Y.; Dai, Y.; Liu, M.; Yu, J.; Wang, C.; Wang, H.; Wang, S.; Zhao, C.; Wu, Y.; Liu, Y. Stimuli-responsive manganese single-atom nanozyme for tumor therapy via integrated cascade reactions. *Angew. Chem., Int. Ed.* **2021**, *60*, 9480-9488.

(2) Wang, Y.; Jia, G.; Cui, X.; Zhao, X.; Zhang, Q.; Gu, L.; Zheng, L.; Li, L. H.; Wu, Q.; Singh, D. J.; Matsumura, D.; Tsuji, T.; Cui, Y.-T.; Zhao, J.; Zheng, W. Coordination number regulation of molybdenum single-atom nanozyme peroxidase-like specificity. *Chem* **2021**, *7*, 436-449.

(3) Chen, D.; Xia, Z.; Guo, Z.; Gou, W.; Zhao, J.; Zhou, X.; Tan, X.; Li, W.; Zhao, S.; Tian, Z.; Qu, Y. Bioinspired porous three-coordinated single-atom Fe nanozyme with oxidase-like activity for tumor visual identification via glutathione. *Nat. Commun.* **2023**, *14*, 7127.

(4) Chen, Q.; Liang, C.; Zhang, X.; Huang, Y. High oxidase-mimic activity of Fe nanoparticles embedded in an N-rich porous carbon and their application for sensing of dopamine. *Talanta* **2018**, *182*, 476-483.

(5) Wang, Y.; Paidi, V. K.; Wang, W.; Wang, Y.; Jia, G.; Yan, T.; Cui, X.; Cai, S.; Zhao, J.; Lee, K.-S.; Lee, L. Y. S.; Wong, K.-Y. Spatial engineering of single-atom Fe adjacent to Cu-assisted nanozymes for biomimetic O_2 activation. *Nat. Commun.* **2024**, *15*, 2239.

(6) Chen, Q.; Li, S.; Liu, Y.; Zhang, X.; Tang, Y.; Chai, H.; Huang, Y. Size-controllable Fe-N/C single-atom nanozyme with exceptional oxidase-like activity for sensitive detection of alkaline phosphatase. *Sens. Actuators, B* **2020**, *305*, 127511.

(7) Xu, Y.; Ma, Y.; Chen, X.; Wu, K.; Wang, K.; Shen, Y.; Liu, S.; Gao, X. J.; Zhang, Y. Regulating reactive oxygen intermediates of Fe−N−C SAzyme via second-shell coordination for selective aerobic oxidation reactions. *Angew. Chem., Int. Ed.* **2024**, *63*, e202408935.

(8) Sun, L.; Yan, Y.; Chen, S.; Zhou, Z.; Tao, W.; Li, C.; Feng, Y.; Wang, F. Co–N–C single-atom nanozymes with oxidase-like activity for highly sensitive detection of biothiols. *Anal. Bioanal. Chem.* **2022**, *414*, 1857-1865.

(9) Xi, J.; Zhang, R.; Wang, L.; Xu, W.; Liang, Q.; Li, J.; Jiang, J.; Yang, Y.; Yan, X.; Fan, K.; Gao, L. A nanozyme-based artificial peroxisome ameliorates hyperuricemia and ischemic stroke. *Adv. Funct. Mater.* **2021**, *31*, 2007130.

(10) Huang, L.; Chen, J.; Gan, L.; Wang, J.; Dong, S. Single-atom nanozymes. *Sci. Adv.* **2019**, *5*, eaav5490.

(11) Liu, X.; Yan, L.; Ren, H.; Cai, Y.; Liu, C.; Zeng, L.; Guo, J.; Liu, A. Facile synthesis of magnetic hierarchical flower-like Co_3O_4 spheres: Mechanism, excellent tetra-enzyme mimics and their colorimetric biosensing applications. *Biosens. Bioelectron.* **2020**, *165*, 112342.

(12) Deng, S.; Hao, Y.; Yang, L.; Yu, T.; Wang, X.; Liu, H.; Liu, Y.; Xie, M. Construction of nanozyme based with mixed valence manganese oxide loaded on defective metal-organic frameworks for sensitive detection of biomarker procalcitonin. *Biosens. Bioelectron.* **2025**, *278*, 117339.

(13) Wei, X.; Chen, J.; Ali, M. C.; Munyemana, J. C.; Qiu, H. Cadmium cobaltite nanosheets synthesized in basic deep eutectic solvents with oxidase-like, peroxidase-like, and catalase-like activities and application in the colorimetric assay of glucose. *Microchim. Acta* **2020**, *187*, 314.

(14) Singh, M.; Bharadwaj, K.; Dey, E. S.; Dicko, C. Sonication enhances the stability of MnO_2 nanoparticles on silk film template for enzyme mimic application. *Ultrason. Sonochem.* **2020**, *64*, 105011.

(15) Lu, W.; Chen, J.; Kong, L.; Zhu, F.; Feng, Z.; Zhan, J. Oxygen vacancies modulation Mn_3O_4 nanozyme with enhanced oxidase-mimicking performance for l-cysteine detection. *Sens. Actuators, B* **2021**, *333*, 129560.

(16) Cheng, H.; Lin, S.; Muhammad, F.; Lin, Y.-W.; Wei, H. Rationally modulate the oxidase-like activity of nanoceria for self-regulated bioassays. *ACS Sens.* **2016**, *1*, 1336-1343.

(17) Li, S.; Hou, Y.; Chen, Q.; Zhang, X.; Cao, H.; Huang, Y. Promoting active sites in MOF-derived homobimetallic hollow nanocages as a high-performance multifunctional nanozyme catalyst for biosensing and organic pollutant degradation. *ACS Appl. Mater. Interfaces* **2020**, *12*, 2581-2590.

(18) Gao, M.; An, P.; Rao, H.; Niu, Z.; Xue, X.; Luo, M.; Liu, X.; Xue, Z.; Lu, X. Molecule-gated surface chemistry of Pt nanoparticles for constructing activity-controllable nanozymes and a three-in-one sensor. *Anal.* **2020**, *145*, 1279-1287.

(19) Cui, M.; Zhao, Y.; Wang, C.; Song, Q. The oxidase-like activity of iridium nanoparticles, and their application to colorimetric determination of dissolved oxygen. *Microchim. Acta* **2017**, *184*, 3113-3119.

(20) Guo, L.; Huang, K.; Liu, H. Biocompatibility selenium nanoparticles with an intrinsic oxidase-like activity. *J. Nanopart. Res.* **2016**, *18*, 74.

(21) Wu, J.; Liu, Q.; Jiao, D.; Tian, B.; Wu, Q.; Chang, X.; Chu, H.; Jiang, S.; Yang, Q.; Liu, T.; Zhang, Y.; Zhang, W.; Fan, J.; Cui, X.; Chen, F. Tensile strain-mediated bimetallene nanozyme for enhanced photothermal tumor catalytic therapy. *Angew. Chem., Int. Ed.* **2024**, *63*, e202403203.

(22) Bhattacharyya, S.; Ali, S. R.; Venkateswarulu, M.; Howlader, P.; Zangrando, E.; De, M.; Mukherjee, P. S. Self-assembled Pd12 coordination cage as photoregulated oxidase-like nanozyme. *J. Am. Chem. Soc.* **2020**, *142*, 18981-18989.

(23) Cao, G.-J.; Jiang, X.; Zhang, H.; Croley, T. R.; Yin, J.-J. Mimicking horseradish peroxidase and oxidase using ruthenium nanomaterials. *RSC Advances* **2017**, *7*, 52210-52217.

(24) Dalapati, R.; Sakthivel, B.; Ghosalya, M. K.; Dhakshinamoorthy, A.; Biswas, S. A cerium-based metal–organic framework having inherent oxidase-like activity applicable for colorimetric sensing of biothiols and aerobic oxidation of thiols. *CrystEngComm* **2017**, *19*, 5915-5925.

(25) Fan, L.; Xu, X.; Zhu, C.; Han, J.; Gao, L.; Xi, J.; Guo, R. Tumor catalytic–photothermal therapy with yolk–shell gold@carbon nanozymes. *ACS Appl. Mater. Interfaces* **2018**, *10*, 4502-4511.

Just Accepted